Structural, Vibrational, and Electronic Study of Sb_2S_3 at High Pressure

J. Ibáñez,[†] J.A. Sans,[‡] C. Popescu,[§] J. López-Vidrier,[†] J.J. Elvira-Betanzos,[†]
V.P. Cuenca-Gotor,[‡] O.Gomis,[°] F.J. Manjón,[*,‡] P. Rodríguez-Hernández,[‖] and A. Muñoz[‖]

[†] Institute of Earth Sciences Jaume Almera, CSIC, 08028 Barcelona, Spain

[‡] Instituto de Diseño para la Fabricación y Producción Automatizada, MALTA Consolider Team, Universitat Politècnica de València, 46022 València, Spain,

[§] ALBA-CELLS, 08290 Cerdanyola del Vallès, Barcelona, Spain

[°] Centro de Tecnologías Físicas: Acústica, Materiales y Astrofísica, MALTA Consolider Team, Universitat Politècnica de València, València, Spain

[‖] Departamento de Física, Instituto de Materiales y Nanotecnología, MALTA Consolider Team, Universidad de La Laguna, 38207 San Cristobal de la Laguna, Tenerife, Spain

Abstract

Antimony trisulfide (Sb_2S_3), found in nature as the mineral stibnite, has been studied under compression at room temperature from a joint experimental and theoretical perspective. X-ray diffraction and Raman scattering measurements are complemented with *ab initio* total-energy, lattice-dynamics, and electronic structure calculations. The continuous changes observed in the volume, lattice parameters, axial ratios, bond lengths and Raman mode frequencies as a function of pressure can be attributed to the different compressibility along the three orthorhombic axes in different pressure ranges, which in turn are related to the different compressibility of several interatomic bond distances in different pressure ranges. The structural and vibrational properties of Sb_2S_3 under compression are compared and discussed in relation to isostructural Bi_2S_3 and Sb_2Se_3. No first-order phase transition has been observed in Sb_2S_3 up to 25 GPa, in agreement with the stability of the *Pnma* structure in Bi_2S_3 and Sb_2Se_3 previously reported up to 50 GPa. Our measurements and calculations do not show evidence either for a pressure-induced second-order isostructural phase transition or for an electronic topological transition in Sb_2S_3.

1. Introduction

Antimony trisulfide (Sb_2S_3) belongs to the A_2X_3 family (A=As, Sb, Bi and X=S, Se, Te) of layered chalcogenide semiconductors with notable thermoelectric properties. Sb_2S_3, known in its mineral form as stibnite, crystallizes at room conditions in the same orthorhombic *Pnma* crystal structure (Fig. 1a) as the minerals antimonselite (Sb_2Se_3) and bismuthinite (Bi_2S_3). In particular, Sb_2S_3 is a semiconductor with a direct bandgap close to 1.75 eV that can be exploited in a wide range of applications, such as photovoltaic cells, optoelectronic devices, fuel cells or gas sensors.[1,2]

The A_2X_3 family has recently attracted a great deal of research attention due to their unique fundamental properties. Noteworthy, three members of this family (Bi_2Te_3, Sb_2Te_3, Bi_2Se_3) have been shown to be 3D topological insulators with a single Dirac cone on the surface.[3,4] This type of compounds represent a new class of matter with insulating bulk electronic states and topologically protected metallic surface states due to time-reversal symmetry and strong spin-orbit interaction which could be applied in spintronics and quantum computation.[5] Furthermore, a recent work has suggested that other member of this family, Sb_2Se_3, becomes a topological superconductor at ~10 GPa and ~2.5 K.[6] Consequently, on account of their fundamental interest and potential topological applications, the quest of new materials with topological insulating or superconducting properties is today one of the hottest topics in condensed matter science, and the investigation of the high-pressure properties of Sb_2S_3 and related compounds is particularly relevant for the search of possible topological states. In addition, the Sb_2S_3-type structure has been recently identified as a possible post-post-perovskite phase in $(Mg,Fe)SiO_3$ minerals.[7] Thus, the study of Sb_2S_3 and its isostructural compounds (Sb_2Se_3 and Bi_2S_3) under compression could provide very useful information about the ultra-high pressure behavior of Earth's mantle minerals.

The properties of Sb_2S_3, Sb_2Se_3 and Bi_2S_3 under compression are also interesting in relation to the stereochemical activity of the A^{3+} ($A=$ As, Sb, Bi) lone-electron pair (LEP) and the occurrence/absence of pressure-induced phase transitions in compounds containing group-15 elements. In particular, a recent high-pressure study on Bi_2S_3 has suggested that a second-order isostructural phase transition (IPT) takes place around 4-6 GPa.[8] Besides, it has been suggested that the IPT is possibly associated to a modification of the Bi_2S_3 electronic structure and related to a pressure-induced electronic topological transition (ETT), also known as Lifshitz transition. Similarly, a pressure-induced ETT has been recently reported in Sb_2S_3 around 4 GPa.[9] These studies are in contrast to a previous study on isostructural Sb_2Se_3, with a smaller bandgap than Sb_2S_3 and Bi_2S_3, which showed no evidence neither of IPT nor of ETT even up to 50 GPa.[10] Furthermore, the claim for the ETTs in Sb_2S_3 and Bi_2S_3 contrasts to previous results reporting a monotonous reduction of the lattice parameters and of the cation lone electron pair (LEP) activity up to 10 GPa in both Sb_2S_3 and Bi_2S_3 without noticing any IPT.[11,12]

The aim of the present work is to study the structural and vibrational properties of Sb_2S_3 at high pressures (HP) and to ascertain the possible existence of a pressure-induced second-order IPT or ETT in this compound. By extension, we aim at understanding the pressure dependence of the properties of the other isostructural (with orthorhombic $Pnma$ structure) sesquichalcogenides, i.e., Sb_2Se_3 and Bi_2S_3. For this purpose, we report a joint experimental and theoretical high-pressure study where high-pressure x-ray diffraction (XRD) and Raman scattering (RS) measurements on

Sb_2S_3 have been performed. Our experiments have been compared and complemented with theoretical calculations of the structural, vibrational and electronic properties of Sb_2S_3 at different pressures. Our XRD results indicate a progressive reduction of the lattice parameters and a smooth change of the values of the atomic positions within the *Pnma* structure, which are accompanied by a strong decrease of the LEP activity of the Sb atoms, in good agreement with the results of Lundegaard et al.[11] We will show that changes observed in the lattice constant ratios, bond lengths and Raman mode frequencies as a function of pressure up to 20 GPa can be attributed to the different compressibility of the material along the three orthorhombic axes, which in turn is related to the different compressibility of various interatomic bond distances in different pressure ranges. We will also show that there is no clear evidence either for a pressure-induced second-order IPT or for an ETT in Sb_2S_3 and that similar conclusions can be drawn with respect to Bi_2S_3 and Sb_2Se_3 below 10 GPa, on the light of the comparison of our theoretical results with previous experimental data.[8,10] Furthermore, we will see that no first-order phase transition is found in Sb_2S_3 up to 25 GPa, in good agreement with previous results for Sb_2Se_3 and Bi_2S_3 up to 50 GPa.[8,10]

2. Experimental details

Synthetic antimony (III) sulfide (Sb_2S_3) powder with grade purity higher than 99.99% was purchased from Sigma-Aldrich. Room-pressure powder XRD, performed with a Rigaku Ultima IV X-ray diffractometer equipped with a Cu tube ($K_{\alpha 1}$ + $K_{\alpha 2}$ lines, ratio 0.5) allowed us to confirm that the available material only contains the stibnite phase.

For high-pressure investigations, a membrane-type diamond anvil cell with 400-μm-diameter culets was used. Powder sample was loaded in a 150-μm-diameter hole drilled in a stainless steel gasket with an initial thickness of 200 μm and preindented to 40 μm. A mixture of 16:3:1 methanol−ethanol−water was used as pressure-transmitting medium. Two room-temperature angle-dispersive powder XRD experiments were performed: the first up to 20 GPa and a second up to 6 GPa to get better data at low pressures in order to improve the data of the equation of state (EOS) of stibnite. Experiments were performed in the BL04-MSPD beamline at ALBA synchrotron facility.[13] This beamline is equipped with Kirkpatrick−Baez mirrors to focus the monochromatic X-ray beam down to 40 x 40 μm^2 and a Rayonix charge-coupled device (CCD) detector with an active area of 165 mm. For the present work, we employed monochromatic radiation with a wavelength of 0.4246 Å and the sample-detector distance was set to 250 mm after calibration with a LaB_6 standard. Pressure was determined with the equation of state (EOS) of metallic Cu, which was intentionally mixed with the Sb_2S_3 powder. Two-dimensional diffraction images were integrated with FIT2D software,[14] while the subsequent structural analysis of the XRD scans was performed

with the program TOPAS 4.2 from Bruker, and also with the PowderCell,[15] and GSAS packages.[16,17]

Room-temperature unpolarized micro-Raman measurements were carried out, up to 26 GPa, with a Horiba Jobin Yvon LabRAM HR spectrometer equipped with a thermoelectrically cooled multichannel CCD detector that enables a spectral resolution better than 2 cm^{-1}. RS measurements were excited with the 6328-Å line of a He:Ne laser with an output power below 5 mW. The Raman signal was collected in backscattering geometry using an edge filter that cuts Raman signals below ~60 cm^{-1} when positioned in perpendicular configuration. Raman shifts down to ~30 cm^{-1} are accessible by properly adjusting the angle between the edge filter and the collected radiation. Pressure was determined with the ruby fluorescence method.[18]

3. Theoretical details

Ab initio total-energy calculations on the orthorhombic *Pnma* structure of Sb_2S_3, Sb_2Se_3 and Bi_2S_3 were carried out within the framework of density functional theory (DFT).[19] The Vienna *Ab-initio* Simulation Package (VASP)[20] was used to perform calculations with the pseudopotential method and the projector augmented waves (PAW) scheme including 6 valence electrons for S ($3s^23p^4$) and for Se ($4s^24p^4$), 15 valence electrons ($4d^{10}5s^25p^3$) for Sb and ($5d^{10}6s^26p^3$) for Bi, respectively. Due to the hardness of the S pseudopotential, the set of plane waves was extended up to a kinetic energy cutoff of 530 eV, providing highly converged results. For Sb_2S_3 and Sb_2Se_3, the exchange-correlation energy was obtained in the generalized gradient approximation (GGA) with the PBEsol prescription.[21] However, for Bi_2S_3 the GGA approach produces an overestimation of the equilibrium volume, so the exchange-correlation energy was described with the AM05 functional.[22] A dense Monkhorst−Pack grid of *k*-special points (2x6x2) was used to perform Brillouin zone (BZ) integrations to ensure high convergence of 1-2 meV per atom in the total energy. Through the calculation of the forces on atoms and the stress tensor, the atomic positions and the unit cell parameters were fully optimized to obtain the relaxed structures at selected volumes. In the relaxed optimized configurations, the resulting forces on the atoms are less than 0.006 eV/Å, with deviations of the stress tensor from hydrostatic conditions (diagonal tensor) lower than 0.1 GPa. The calculations provide not only a set of structural parameters as a function of pressure, but also a set of accurate energy, volume and pressure data that are fitted using an equation of state in order to obtain the equilibrium volume, the bulk modulus and its pressure derivatives.

Electronic band-structure calculations were carried out at different pressures along selected paths on the first BZ. In turn, lattice-dynamics calculations were performed at the zone center (Γ point) and along high-symmetry directions of the BZ as a function of pressure using the direct-force

constant approach.[23] The construction of the dynamical matrix at the Γ point of the BZ involves separate calculations of the forces that result from a fixed displacement away from equilibrium of the atoms in the primitive cell. The diagonalization of the dynamical matrix provides the normal-mode frequencies. Moreover, these calculations allow identifying the irreducible representations and the character of the vibrational phonon modes at the Γ point. To obtain the phonon dispersion curves and the phonon density of states (DOS), we performed similar calculations using appropriate supercells.

4. Results

4.1. Structural and vibrational characterization of Sb_2S_3 at room conditions

Sb_2S_3 crystallizes at room pressure in an orthorhombic crystal, space group *Pnma* (Z=4, U_2S_3-type), where all atoms are located at 4c Wyckoff positions. Figure 2a shows the XRD pattern of Sb_2S_3 at room pressure. The experimental lattice and atomic parameters obtained from a Rietveld refinement are summarized in Table 1, where our calculated lattice atomic parameters 0 K are also provided for comparison. Our experimental results are very similar to those recently reported by Kyono et al.[24] It can also be observed that our theoretical *a* and *b* values are very close to our experimental results (difference below 1%), while the theoretical *c* value is the parameter more deviated from experimental results. The difference between the experimental and calculated value for the *c* axis is less than 3.5%, which is typical of GGA calculations. We have to note that our theoretical values are similar to those recently calculated by *ab initio* methods.[2,25]

At room pressure, Sb atoms in Sb_2S_3 occupy two distinct positions, namely Sb(1) and Sb(2), each of which is bonded to three S atoms with short bonds (< 2.7 Å) and to four additional S atoms with longer bonds, resulting in an apparent sevenfold coordination. However, at room pressure the actual coordination is smaller, as illustrated in Fig. 1a. The shortest Sb-S bonds give rise to distorted trigonal SbS_3 units (Sb(1) atoms) and tetragonal SbS_5 pyramids (Sb(2) atoms), leading to SbS_3E tetrahedra and SbS_5E octahedra of quasi-fourfold and quasi-sixfold coordination, respectively (E indicates the LEP of both Sb atoms). Note that SbS_3 units have one Sb(1)-S(2) and two Sb(1)-S(1) bonds of 2.558 and 2.569 Å, respectively, leading to an average Sb-S bond distance of 2.565 Å. In turn, SbS_5 units are composed of Sb(2)-S(3), Sb(2)-S(2) (2×), and Sb(2)-S(3)(2×) bonds of 2.499, 2.664 and 2.842 Å, respectively, leading to an average Sb-S bond distance of 2.703 Å. The larger average Sb-S bond distance in SbS_5 units is consistent with the larger coordination with respect to SbS_3 units and supports the cation coordinations at room pressure shown in Fig. 1a. Stacking of SbS_3 and SbS_5 units yield a crumpled sheet-type disposition with infinite $(Sb_4S_6)_n$ units resulting in

layers extending mainly in the *b-c* plane and piled up mainly along the *a* axis. This description of the structure of Sb_2S_3 is similar for isostructural compounds Sb_2Se_3 and Bi_2S_3.

As regards lattice dynamics, group theory predicts 60 zone-center phonon modes for Sb_2S_3 belonging to the following irreducible representations: $\Gamma = 10A_g + 5B_{1g} + 10B_{2g} + 5B_{3g} + 5A_u + 10B_{1u} + 5B_{2u} + 10B_{3u}$. Three of these modes ($B_{1u}$, B_{2u} and B_{3u}) correspond to acoustic phonons and A_u modes are silent modes. There are 30 Raman-active (R) optical modes ($\Gamma = 10A_g + 5B_{1g} + 10B_{2g} + 5B_{3g}$) and 22 infrared-active (IR) optical modes ($\Gamma = 9B_{1u} + 4B_{2u} + 9B_{3u}$). Figure 2b shows the room-pressure unpolarized RS spectrum of Sb_2S_3 together with the position of all the calculated Raman-mode frequencies. As observed, the RS spectrum shows a mixture of narrow and broad bands between 35 and 320 cm^{-1}. Our experimental and theoretical results (see Table 2) are in good agreement with recently reported polarized RS spectra and calculations at room conditions.[26] It must be noted that the RS spectrum of natural (stibnite) or synthetic Sb_2S_3 at room conditions has been the subject of several previous works. However, most of the reported RS spectra correspond to laser-damaged samples as discussed by Kharbish et al.[27] Therefore, most of the RS spectra of this compound at room conditions reported to date are not valid with the exception of recent measurements.[26]

The large number of Raman-active modes in our RS spectrum at room pressure and the broadening of experimental peaks makes their identification, using only the RS spectrum at room pressure with the help of *ab initio* calculations, almost impossible. However, we will show later that the knowledge of the experimental and theoretical pressure coefficients of the different Raman modes helps in the tentative assignment of the symmetries of some of the modes, as summarized in Table 2.

In general, most optical vibrational modes in Sb_2S_3 include displacement of both Sb and S atoms due to the complex structure and low symmetry of Sb_2S_3. In this respect, the modes with low frequencies (<150 cm^{-1}) should be mainly contributed by the movement of heavy Sb atoms, while the modes with high frequencies are expected to be mainly determined by the displacement of light S atoms. As observed in Table 2, all our theoretically calculated vibrational modes come in pairs: ($B_{1g}+B_{3g}$) and (A_g+B_{2g}) in the case of Raman-active modes, and (A_u+B_{2u}) and ($B_{1u}+B_{3u}$) in the case of the IR phonons. In ($B_{1g}+B_{3g}$) and (A_u+B_{2u}) modes, atoms vibrate along the *b* axis, i.e., the main direction along which the layers extend. In turn, in (A_g+B_{2g}) and ($B_{1u}+B_{3u}$) modes the atoms vibrate in directions perpendicular to the *b* axis. The relation between the structural SbS3E and SbS5E units and vibrational modes in stibnite is more extensively described in the Supporting Information.

4.2. High-pressure XRD measurements

Angle-dispersive XRD patterns of Sb_2S_3 at selected pressures are shown in Fig. 3a. As observed, all diffraction peaks exhibit the expected shift to larger angles upon compression as a consequence of the pressure-induced decrease of interplanar distances. Figure 3b shows an example of a Rietveld refinement inside the diamond anvil cell for the pattern at 2.9 GPa. No phase transition was observed up to 20 GPa, in good agreement with a recent study on slightly As-doped stibnite up to 25.7 GPa.[28] Above 7 GPa, the XRD scans display strong signal from Cu (see pattern at 10.8 GPa), so we were not able to extract information about the atomic positions with Rietveld refinements above this pressure. In this sense, we measured in two different regions at each pressure: one with most of the signal coming from the sample (to characterize our sample in optimal conditions) and another region with a huge calibrant signal (to obtain a precise value of the pressure inside the diamond anvil cell). However, the sample cavity becomes smaller with increasing pressure and the signal coming from both (sample+calibrant) get mixed in our experiment above 10 GPa.

Figure 4 shows the volume vs. pressure data as obtained from our experiment and from our theoretical calculations. A fit of experimental and theoretical data to a third-order Birch−Murnaghan EOS allows us to obtain the zero-pressure volume (V_0), bulk modulus (B_0), and its pressure derivative (B_0'), which are summarized in Table 3. Our experimental bulk modulus (B_0 = 37.6(2) GPa with B_0'=3.8(7)) is only slightly larger than our theoretical value (B_0= 32.2 GPa with B_0'= 6.2). Lundegaard *et al.* obtained a smaller value (B_0= 26.9 GPa) from high-pressure single-crystal XRD measurements in stibnite samples,[11] although with a much larger pressure derivative value (B_0'=7.9, twice larger than the value obtained in the present work). Similarly, a value B_0= 28.2 GPa with B_0'=3.1 has been recently reported for slightly As-doped stibnite from energy-dispersive XRD measurements.[28]

For a better comparison with isostructural compounds, a fit of our experimental data by fixing the experimental B_0' value to our theoretical one (6.2) yields B_0 = 33.3(3) GPa, which is in better agreement with previous experimental data and also with our theoretical results. The value of our experimental bulk modulus for Sb_2S_3 is similar to that of Sb_2Se_3 (B_0= 30(1) GPa with B_0'= 6.1(2)) **[10]** and Bi_2S_3 (with average values of B_0= 37.5 GPa and B_0'=6.0(5)).[8,12] Furthermore, our calculated bulk modulus for Sb_2S_3 is of the same order than the recently calculated value for Bi_2S_3.[29] Note that the above results on the three isostructural compounds show a disagreement with other bulk moduli theoretically calculated,[25,30] which seem to be largely overestimated.

The pressure dependence of the experimental and theoretical lattice parameters (*a*, *b*, and *c*) of Sb_2S_3 is plotted in Fig. 5a. The experimental lattice parameters obtained from the XRD pattern at room conditions are also shown. As can be seen, the theoretical results closely follow our

experimental data, although with the slight underestimation of the c parameter commented in the previous section. Interestingly, the experimental curves corresponding to the a and c parameters cross each other at around 1 GPa due to the larger compressibility of Sb_2S_3 along the a axis than along the c axis at very low pressures. This result is in good agreement with data reported by Lundegaard et al.[11]

By fitting the experimental and theoretical data of Fig. 5a with a modified Birch-Murnaghan EOS,[31] we obtain the axial bulk modulus at room pressure for the a, b, and c lattice parameters summarized in Table 3. Our experimental axial bulk moduli values are consistent, although slightly larger, than those reported by Lundegaard et al.[11] They are also similar to that of the b axis reported for slightly As-doped stibnite by Fan et al.;[28] however, the values of the bulk moduli for the a and c axes in the latter work are clearly in disagreement with those of Lundegaard et al. and also with our results. At present, we have no explanation for this disagreement, but these differences cannot be ascribed to the presence of As (3%) in the natural stibnite samples[28] since all three works (ours and Refs. 11 and 28) report the expected larger bulk modulus of the b axis of Sb_2S_3 relative to the a and c axes. This result is clearly due to the fact that the $(Sb_4S_6)_n$ units extend along the b axis forming rods and, as a consequence, the main forces present along the b axis are strong covalent Sb-S bonds. On the other hand, the bulk moduli of Sb_2S_3 along the a and c axes are much smaller than that of the b axis, being the bulk modulus of the c axis larger than that of the a axis. This behavior can be explained because the rods extending along the b axis are also linked by weak Sb-S forces along the c axis forming distorted layers, while the resulting layers are stacked along the a axis where they are bonded by much weaker van der Waals forces. The slightly smaller bulk modulus of Sb_2S_3 along the a axis than along the c axis is also related to the presence of cation LEPs, which point closer to the [100] direction than to the [001] direction.

With regard to isostructural compounds Sb_2Se_3 and Bi_2S_3, the compressibilities of a, b and c axes at room pressure in Sb_2S_3 are similar to those previously reported for Sb_2Se_3 and Bi_2S_3 (see Table 4). This result is consistent with the similar bulk modulus of the three compounds previously mentioned, which suggests that the explanation given in the previous paragraph to explain the different axial bulk moduli in Sb_2S_3 is also valid for Sb_2Se_3 and Bi_2S_3.

As already commented, a pressure-induced IPT related to a change in the electronic band structure, and which could correspond to a pressure-induced ETT, has been recently suggested in Bi_2S_3 and Sb_2S_3.[8,9] An ETT or Lifshitz transition is produced when band extrema of the electronic band structure, associated with a Van Hove singularity in the electronic density of states (EDOS), cross the Fermi level thus changing the topology of the Fermi energy surface.[32] Under these conditions, the strong redistribution of the EDOS at the Fermi level gives rise to a $2^{1/2}$-order IPT at

0 K in the Ehrenfest classification. The ETT does not cause a discontinuity in the volume or in the Wyckoff positions, but it leads to anomalies in mechanical, vibrational, thermodynamic and electrical properties.[33] ETTs in metals are well known for many years,[34] but recently ETTs have been observed in some small-bandgap semiconductors, as reviewed in the case of Bi_2Te_3, Sb_2Te_3, Bi_2Se_3 at high pressures.[35] Pressure-induced changes of the bulk modulus, B_0, and of the slope sign in the c/a axial ratio of Bi_2Te_3, Sb_2Te_3 and Bi_2Se_3 have been observed and related to high values (>4) of B_0'. Consequently, the presence of minima in the axial ratios with increasing pressure in other A_2X_3 compounds has been associated to the occurrence of a pressure-induced ETT. Recently, this hypothesis has been put into question since such minima could correspond to the presence of an IPT or just to changes in the compressibility of different bonds in layered compounds but without being related to an ETT.[36] In fact, no change of structural parameters has been observed for the recently reported pressure-induced ETT in black phosphorous.[37,38] For the sake of comparison with previous studies of A_2X_3 compounds, we show in Fig. 5b the experimental and theoretical a/b, c/b, and a/c axial ratios as a function of pressure in Sb_2S_3. As can be seen, there is a strong decrease of a/b and a/c axial ratios at low pressures with a minimum in the theoretical a/c ratio around 6 GPa, which is not observed in our experiment. However, this minimum around 5 GPa in Sb_2S_3 has been reported by Sorb et al.[9] with experimental data taken from Lundegaard et al.[11] Similarly, minima in axial ratios have been observed in isostructural compounds Bi_2S_3 and Sb_2Se_3 around 4 GPa and 10 GPa, respectively.[8,10]

We have to stress that the minimum of the c/a ratio found in Bi_2Te_3, Sb_2Te_3 and Bi_2Se_3 compounds with layered tetradymite structure plays the role of the a/b ratio in the stibnite structure. Note that this is the axial ratio between interlayer and intralayer bond distances; i.e., the ratio between weak van der Waals and strong covalent interactions. In this regard, no clear minimum has been observed either experimentally or theoretically for the a/b axial ratio in Sb_2S_3, unlike in isostructural compounds Bi_2S_3 and Sb_2Se_3, where a minimum has been reported near 4 and 15 GPa, respectively.[8,10] The fact that a minimum in the a/b ratio is found in these two compounds, but no minimum has been observed in black phosphorous,[37] suggests that the behavior of the axial ratio alone does not provide a clear evidence for the existence of a pressure-induced ETT.

Second-order IPTs, not necessarily associated to an ETT but solely arising from a strong pressure-induced decrease in the activity of the LEP have also been recently reported. This is the case of other binary compounds involving group-15 and group-16 atoms such as tetragonal β-Bi_2O_3.[39] In this case, a large B_0' and a change in the c/a ratio, accompanied with an increase of symmetry of all occupied Wyckoff sites, has been observed.[39] To evaluate the possibility of an IPT of this kind in Sb_2S_3, we have examined the experimental (up to 7 GPa) and calculated evolution of

the Sb Wyckoff positions (Fig. 6a) together with the calculated pressure dependence of the Sb(1)-S and Sb(2)-S bond lengths (Fig. 6b and Fig. 6c).

As can be seen in Fig. 6a, there is a smooth change of the Sb atomic positions with increasing pressure. A good agreement between refined and calculated Sb coordinates is observed. An overall good agreement is also found for S atomic positions (not shown), although the error of the refined S sites was larger than for Sb sites. As observed, the x coordinate of the Sb(1) site becomes negative above 5 GPa (experimentally) and above 9 GPa (theoretically), but do not tend to zero. Similarly, other coordinates of Sb do not tend either to a more symmetric (or asymmetric) position with increasing pressure. Consequently, our results indicate that there is no net change in symmetry in the atomic Wyckoff positions of Sb_2S_3 with increasing pressure. Therefore, no pressure-induced IPT from a low symmetry phase to a high symmetry phase (or vice versa) seems to occur up to 20 GPa in Sb_2S_3.

The monotonous change in the atomic positions with increasing pressure found by our calculations, and confirmed by our experiments up to 7 GPa, leads to a monotonous change in the Sb(1)-S and Sb(2)-S bond lengths up to 20 GPa as shown in Fig. 6b and Fig. 6c, respectively. This smooth reduction of the average Sb(1)-S and Sb(2)-S distances with pressure leads to more regular polyhedral units upon compression. This is illustrated in Fig. 1b and Fig. 1c, which show the unit-cell of Sb_2S_3 at 6.3 and 21.2 GPa, respectively, for comparison with that at room pressure (Fig. 1a). As can be seen in Fig. 1, the main effect of the reduced distance between Sb and S sites is the transformation of the SbS_3E and SbS_5E units into SbS_7 units above 20 GPa. However, the strong decrease of Sb(1)-S distances at low pressures leads to an intermediate coordination with distorted SbS_6 units above 6 GPa.

A similar behavior of the cation-anion distances under compression is observed in Bi_2S_3 and Sb_2Se_3 (see Figs. S1 and S2 in the Supporting Information) due to the decrease of the activity of the cation LEP with increasing pressure. This result is in good agreement with what happens in other group-15 sesquioxides and sesquichalcogenides. For the sake of consistence, a comparison of experimental and theoretical values of lattice and atomic parameters for Sb_2Se_3 and Bi_2S_3 at room pressure are given in Tables S1 and S2 in the Supporting Information. In the case of Bi_2S_3, our *ab initio* structural calculations (Fig. S1), which have been performed at more pressure values than the experimental points shown by Efthimiopoulos *et al.*[8] suggest a progressive and smooth change of the different Bi-S bond lengths in Bi_2S_3 upon compression. Our theoretical results and subsequent interpretation are consistent with the experimental data of Lundegaard *et al.*[12] In that work, a monotonous evolution of the Bi-S bond lengths resulting in sevenfold cation coordination above 10 GPa, together with a smooth reduction of the LEP volume, was reported. Similarly, our theoretical

results for Sb_2Se_3 (Fig. S2) suggest a progressive and smooth change of the different Sb-Se bond lengths upon compression that also result in sevenfold cation coordination above 10 GPa, in good agreement with experimental data.[10] Thus, no abrupt changes that could be related to any second-order IPT is observed in any of the three isostructural compounds Sb_2S_3, Sb_2Se_3 and Bi_2S_3.

In summary, the compression of Sb_2S_3 is characterized by progressive structural changes that lead from a layered structure at room pressure (with quasi-fourfold and quasi-sixfold coordinated Sb atoms) to a quasi-3D structure above 20 GPa (with sevenfold coordinated Sb atoms). Similar conclusions are reached in the case of Bi_2S_3 and Sb_2Se_3, where sevenfold cation coordination is attained at a smaller pressure (around 10 GPa). These changes do not involve any major change in atomic Wyckoff sites and are mainly related to the reduction of the LEP activity of Sb/Bi atoms with increasing pressure. All three isostructural compounds (Sb_2S_3, Sb_2Se_3 and Bi_2S_3) show rather similar structural behavior under pressure; no clear confirmation of the presence of a pressure-induced IPT has been found. Therefore, we cannot confirm the recently reported [9] presence of a pressure-induced ETT only from structural data.

4.3 High-pressure Raman measurements

We have also performed high-pressure RS measurements on Sb_2S_3 in combination with DFT lattice-dynamical calculations in order to better understand the behavior of this compound under compression and gain still further insight about a possible pressure-induced IPT or ETT. As demonstrated in numerous previous investigations, RS measurements are highly sensitive to detect IPTs in chalcogenide compounds even for the most elusive ETTs. Anomalies in the experimental pressure coefficients and widths of different Raman peaks have been reported around the ETT in Bi_2Te_3,[40] Sb_2Te_3,[41] and Bi_2Se_3.[42] Other IPTs related to the LEP activity, like those found in β-Bi_2O_3 [39] or cubic α-Sb_2O_3,[43] also show clear changes in the pressure coefficient of several soft modes around the phase transition that also correlate with anomalies of the peak widths and intensities.

We have plotted in Fig. 7 room-temperature RS spectra of Sb_2S_3 at selected pressures. We would like to note that there is an overall intensity reduction of the Raman signal above ~15 GPa that does not affect the evolution of the observed Raman features with pressure. The decrease of the Raman intensity could be attributed to the gap decrease as will be explained in the following section. We would also like to note that our RS spectra at different pressures are rather different to those recently reported by Sorb et al.,[9] excited with 532-nm light and which most likely correspond to laser damaged samples due to laser absorption, as suggested by Sereni et al.[26] in relation to older works. Thus, taking into account our present results, we conclude that the Raman data reporting

evidence for a pressure-induced ETT in Sb_2S_3 [9] must be revisited since conclusions reached from laser-damaged samples must be taken with caution, as discussed by Kharbish et al.[27]

As already mentioned, it is very difficult to assign the features that show up in the room-pressure RS spectrum of Sb_2S_3 (see Fig. 2b) due to strong overlapping. However, it is possible to perform a tentative peak assignment by studying the pressure behavior of the Raman-active peaks in combination with the results of lattice-dynamical calculations. Figure 8 shows the pressure dependence of the experimental and theoretical Raman-active mode frequencies of Sb_2S_3. In general, both experimental and theoretical Raman modes do not show a simple monotonic behavior with increasing pressure; however, some of the theoretical curves in Fig. 8 closely match the experimental data. This is particularly clear in the case of A_g modes, which exhibit in several cases a remarkable agreement between theory and experiment. For the rest of symmetries, although the assignments bear some degree of ambiguity, our DFT lattice-dynamical calculations reproduce rather well the overall pressure behavior of experimental Raman-active modes in Sb_2S_3. Table 2 summarizes the experimental and theoretical frequencies at room pressure (ω_0) and the pressure coefficients as obtained from fits of experimental and theoretical Raman-mode frequencies reported in Fig. 8 as a function of pressure (P) to the equation $\omega(P) = \omega_0 + \alpha \cdot P + \beta \cdot P^2$. The assignments of the features that appear in the RS spectrum of Sb_2S_3 are reported in Table 2 and Figure 8.

It is noteworthy that some of the Raman-active modes of Sb_2S_3 exhibit moderate softening in a given pressure range, others mix and/or cross other modes, while others display complex anti-crossing behavior. However, neither the experimental points nor the theoretical curves seem to display a markedly anomalous behavior around any specific pressure value. Instead, the observed evolution of the modes may be ascribed to the progressive pressure-induced changes in atomic positions and bond lengths. Consequently, our high-pressure RS measurements do not provide clear evidence for an IPT or ETT in Sb_2S_3 as in the case of the results obtained by XRD.

In order to confirm that no second-order IPT is observed in Sb_2S_3 we have calculated the phonon dispersion curves of Sb_2S_3 at several pressures up to 20 GPa (not shown). In the pressure range studied, no soft-mode behavior that could be indicative of a second-order IPT is observed in this compound up to 20 GPa. This result for Sb_2S_3, extended to the case of the isostructural compounds Sb_2Se_3 and Bi_2S_3, is in agreement with recent calculations of the elastic constants of Bi_2S_3 as a function of pressure, which indicated that this compound is stable up to 10 GPa.[29]

As regards the comparison of our RS results with those in Bi_2S_3 and Sb_2Se_3, our RS results contrast with those in Bi_2S_3, where some anomalies in the 6-10 GPa range, well above the region corresponding to the minimum in the c/a ratio (4 GPa), have been reported.[8] In order to further understand the pressure behavior of isostructural compounds, we have performed lattice-dynamics

calculations in Bi_2S_3 and compared the results with the reported RS measurements (see Fig. S3 in the Supporting Information). Despite a clear assignment of experimental Raman-active modes of Bi_2S_3 on the basis of our calculations is difficult, the comparison of the pressure dependence of the experimental and theoretical Raman-active phonons of Bi_2S_3 is very similar to that of Sb_2S_3, i.e., a non-monotonic behavior of the Raman-active modes is observed, with some modes showing a certain softening followed by crossings and anti-crossings, but with no clear evidence of a general change at a certain pressure value. This behavior of Raman-active modes in Bi_2S_3 is consistent with the progressive repositioning of the atoms within the orthorhombic *Pnma* unit cell and a progressive overall decrease of average Bi-S bond lengths (see Fig. S1), leading to more regular polyhedral units and highly coordinated Bi atoms as already commented. Consequently, our results and analysis suggest that most of the anomalies reported in Bi_2S_3 by Efthimiopoulos *et al.*[8] may actually correspond either to the non-linear behavior of several Raman-active modes with pressure or to phonon modes that undergo crossings and anti-crossings upon compression, which are difficult to analyze without the help of theoretical calculations. An example of this latter case is the crossing of the $B_{1g}(2)$ and $A_g(2)$ near 200 cm^{-1} between 7 and 10 GPa (according to notation of Efthimiopoulos *et al.*) which likely correspond to the crossing of B_{1g} and B_{3g} modes predicted by the calculations (see Fig. S3).

Regarding Sb_2Se_3, the behavior of first-order Raman-active modes up to 300 cm^{-1}, with crossings at different pressures, has been reported up to 45 GPa without observation of any pressure-induced IPT or ETT.[10] We show in Fig. S4 in the Supporting Information the pressure dependence of the Raman-active mode frequencies as a function of pressure, where our theoretically calculated modes are compared to experimental frequencies reported in the literature. Noteworthy, a smaller number of Raman-active modes has been measured in Sb_2Se_3 than in Sb_2S_3 and Bi_2S_3. No clear assignment of experimental Raman-active modes of Sb_2Se_3 on the basis of our calculations is possible, most likely because the experimental Raman features actually arise from a mixture of different Raman modes with close frequencies. As predicted by our calculations, strong overlapping is particularly expected in Sb_2Se_3 between 100 and 200 cm^{-1}. As can be seen in Fig. S4, the theoretical Raman-active modes exhibit a non-monotonic behavior with some modes showing a certain softening followed by crossings and anti-crossings, but with no clear evidence of a general change at any particular pressure value as in the previous isostructural compounds. In fact, the number of crossings and anticrossings in Sb_2Se_3 is much larger than in Sb_2S_3 and Bi_2S_3 because of the large number of Raman-active modes located in a narrow frequency range due to the larger mass of Se than of S. Again, the behavior of Raman-active modes in Sb_2Se_3 is consistent with a progressive repositioning of the atoms within the orthorhombic *Pnma* unit cell and a progressive

overall decrease of Sb-Se bond distances (Fig. S2), leading to more regular polyhedral units and highly coordinated Sb atoms as already commented.

In summary, RS measurements of Sb_2S_3 show a complex behavior of phonon modes with increasing pressure. However, there is no clear evidence of a sudden change at a defined pressure that could be attributed to the presence of an IPT or an ETT. Our lattice-dynamical *ab initio* calculations for isostructural Bi_2S_3 and Sb_2Se_3 show that previously reported results for these two compounds may be interpreted in the same way as for Sb_2S_3. Thus, we conclude that all three isostructural compounds (Sb_2S_3, Sb_2Se_3 and Bi_2S_3) exhibit rather similar vibrational properties under compression, again with no clear confirmation of the presence either of a pressure-induced IPT or ETT.

4.4 Electronic structure calculations

Since ETTs are very subtle transitions, we have performed band-structure calculations in Sb_2S_3 at different pressures in order to identify possible changes of the band extrema that could be related to an ETT. We show in Fig. 9 the electronic band structure at 0, 1.0, 3.9, and 6.3 GPa. As can be seen, the predicted structure at ambient pressure exhibits a quasi-direct fundamental bandgap (theoretical value around 1.1 eV), since the conduction band minimum (CBM) and valence band maximum (VBM) are located in the Z-Γ direction at slightly different wavevectors. However, the energy of the predicted indirect bandgap is close to that of the direct bandgap at Γ. This picture is similar to that previously reported and reviewed in calculations of Sb_2S_3 at room pressure.[2]

With increasing pressure, the bandgap closes and both the VBM and the CBM move progressively toward the Γ point. Around 1 GPa, our calculations show that the CBM is already located at the Γ point, but the bandgap remains indirect. Above 4 GPa the VBM is already located at the Γ point and the bandgap becomes fully direct. This result could explain the change in the electric resistivity measurements around 4 GPa recently reported.[9] Notwithstanding, this change in electrical resistivity must be taken with caution because it has been measured in compacted powders with randomly-oriented grains and not in single crystals with well-defined faces. In this way, the measured resistivity represents an average along the three orthorhombic axes and additionally is affected by inter-grain connections whose effect is unknown. At higher pressures, the direct bandgap exhibits a progressive closing and no other relevant changes are predicted by our calculations. The perspective offered by our theoretical calculations of the pressure dependence of the electronic band structure in Sb_2S_3 is in good agreement with that provided by prior photoelectric measurements under pressure.[44] In this regard, we have to note that although DFT calculations underestimate the bandgap value, its pressure coefficient is well described. Thus, we estimate that

the direct bandgap of Sb_2S_3 should close at pressures beyond 14-15 GPa taking into account the small pressure coefficient of the direct bandgap above 4 GPa. Consequently, it is possible that the strong decrease of the Raman signal we have measured above 14 GPa could be related to the strong decrease and even closure of the bandgap above this pressure.

As can be seen in Fig. 9, the evolution of the electronic structure is progressive and relatively smooth, and therefore the change of the EDOS around the Fermi level with pressure is expected to be very small. Thus, it can be concluded that the calculated pressure-induced variation of the electronic band structure of Sb_2S_3 is that of a conventional semiconductor and does not exhibit any sizable change in the EDOS around the Fermi level that could be linked to an ETT. Therefore, our calculations do not support the occurrence of a pressure-induced ETT in Sb_2S_3.

For the sake of completeness, we have also performed electronic band structure calculations including spin-orbit coupling (SOC) in Bi_2S_3 and Sb_2Se_3 at different pressures (see Figs. S5 and S6 in the Supporting Information). Our calculations show that these two semiconductors have also rather large bandgaps, around 1.15 eV and 0.75 eV for Bi_2S_3 and Sb_2Se_3, respectively. These results agree qualitatively with those of recent GW calculations, which yield energies of 1.5 eV (Sb_2S_3), 1.4 eV (Bi_2S_3) and 1.3 eV (Sb_2Se_3), which should be closer to real values.[2] Our calculations show that the bandgap decreases in the three isostructural compounds with increasing pressure; the bandgap closes above 10-15 GPa in all three compounds, being Sb_2Se_3 the first one to become metallic above 10 GPa and Sb_2S_3 the last one to become metallic above 15 GPa.

As in the case of Sb_2S_3, we are not able to identify any anomalies in Bi_2S_3 and Sb_2Se_3 around the band extrema at low pressures that could be related to an ETT. In Bi_2S_3, a change of the VBM from the Γ-X to the Γ-Z direction is observed near 3.5 GPa, with a calculated bandgap value around 1 eV. Calculations for Bi_2S_3 predict that this compound has a pseudo-direct bandgap up to larger pressure values than Sb_2S_3. The bandgap closes with increasing pressure as in Sb_2S_3, but is wide open up to pressure values well above 10 GPa. Therefore, the electronic structure only shows smooth changes and, consequently, we can safely conclude that the change of the EDOS around the Fermi level with pressure may be expected to be very small, with no ETT expected to occur in this compound around 4-6 GPa. As regards Sb_2Se_3, our calculations predict that this compound has a direct or quasi-direct bandgap, whose VBM and CBM are located along the Γ-Z direction at room pressure. The calculations predict a change of the CBM from the Γ-Z to the Γ-Y direction above 1 GPa, for which the calculated bandgap value is around 0.65 eV and the real value must be above 1 eV. The new indirect bandgap closes progressively with increasing pressure and decreases below 0.5 eV above 3 GPa, but is wide open up to pressure values above 10 GPa. Hence, our calculations allow us to explain the conducting behaviour of Sb_2Se_3 observed by Kong *et al.* between 3 and 10

GPa,[6] if we consider that their samples have a considerable unintentional carrier concentration due to non-stoichiometry, which can contribute to electrical conductivity as the bandgap closes. The electronic band structure of Sb_2Se_3 shows smooth changes up to 10 GPa. Thus, we conclude that the change with pressure of the EDOS around the Fermi level may be expected to be very small near 1 GPa, with no ETT expected to occur in this compound.

In summary, our electronic band structure calculations show some changes in the CBM and VBM of the three isostructural compounds Sb_2S_3, Bi_2S_3 and Sb_2Se_3 at low pressures. At such pressure values the bandgap of the three compounds is wide open (above 0.6 eV), and therefore any changes of the EDOS around the Fermi level may be expected to be very small to yield a pressure-induced ETT as claimed in previous works.

5. Conclusions

We have reported a joint experimental and theoretical study of Sb_2S_3 under compression. Our study indicates that its quasi-laminar orthorhombic *Pnma* structure undergoes progressive and monotonic changes of lattice parameters and atomic positions with increasing pressure resulting in a quasi-3D material above 20 GPa. This structural change is consistent with an overall increase of Sb coordination and with a decrease of the lone electron pair activity of Sb upon compression. In this way, Sb_2S_3 is composed of SbS_3 and SbS_5 polyhedral units at room pressure, which become distorted SbS_7 polyhedra at pressures above 20 GPa. The continuous changes observed in the axial ratios, bond lengths and Raman mode frequencies as a function of pressure of Sb_2S_3 can be attributed to the different compressibility along the three orthorhombic axes, which in turn are related to the different compressibility of the interatomic forces in different pressure ranges. We have found no clear evidence either for a second-order IPT or for an ETT in Sb_2S_3 at low pressures. The same conclusion can be drawn for isostructural Bi_2S_3 and Sb_2Se_3 on the light of the comparison of our theoretical results with previous experimental data. Furthermore, no first-order phase transition has been observed in Sb_2S_3 up to 25 GPa, in good agreement with the stability of the *Pnma* structure in Bi_2S_3 and Sb_2Se_3 previously reported up to 50 GPa.

In summary, our joint experimental and theoretical work allows us to conclude that the three isostructural compounds Sb_2S_3, Bi_2S_3, and Sb_2Se_3 exhibit similar structural and vibrational properties with increasing pressure, with no pressure-induced ETT in the low pressure regime (below 10 GPa) despite the decrease upon compression of the direct and indirect bandgap values in all three compounds.

ASSOCIATED CONTENT

Supporting Information

The Supporting Information is available free of charge on the ACS Publications website at DOI:…..

Explanation of vibrational properties of Sb_2S_3 as well as structural, vibrational, and electronic calculations of Sb_2Se_3 and Bi_2S_3 at different pressures compared to experimental values from other works. (PDF)

AUTHOR INFORMATION

Corresponding Author

*E-mail: fjmanjon@fis.upv.es. Telephone: (+34) 963877000 ext (75287).

Author Contributions

The manuscript has been written through contributions of all authors. All authors have given approval to the final version of the manuscript.

Notes

The authors declare no competing financial interest.

References

[1] Moon, S.-J.; Itzhaik, Y.;Yum, J.-H.;, Zakeeruddin, S. M.; Hodes, G.; Grätzel, M. Sb_2S_3-Based Mesoscopic Solar Cell using an Organic Hole Conductor. *J. Phys. Chem. Lett.*, **2010**, *1*, 1524–1527.

[2] Filip, M. R.; Patrick, Ch. E.; Giustino, F. GW Quasiparticle Band Structures of Stibnite, Antimonselite, Bismuthinite, and Guanajuatite *Phys. Rev. B* **2013**, *87*, 205125.

[3] Chen, Y. L.; Analytis, J. G.; Chu, J. H.; Liu, Z. K.; Mo, S.K.; Qi, X. L.; Zhang, H. J.; Lu, D. H.; Dai, X; Fang, Z.; et al. Experimental Realization of a Three-Dimensional Topological Insulator, Bi_2Te_3. *Science* **2009**, *325*, 178-181.

[4] Zhang, H.; Liu, C. X.; Qi, X. L.; Dai, X.; Fang, Z.; Zhang, S. C. Topological Insulators in Bi_2Se_3, Bi_2Te_3 and Sb_2Te_3 with a Single Dirac Cone on the Surface. *Nat. Phys.* **2009,** *5*, 438-442

[5] Hasan, M. Z.;Kane, C. L. Colloquium: Topological Insulators. *Rev. Mod. Phys.* **2010,** *82*, 3045-3069.

[6] Kong, P. P.; Sun, F.; Xing, L. Y.; Zhu, J.; Zhang, S. J.; Li, W. M.; Liu, Q. Q.; Wang, X. C.; Feng, S. M.; Yu, X. H.; et al. Superconductivity in Strong Spin Orbital Coupling Compound Sb_2Se_3. *Sci. Rep.* **2014,** *4*, 6679-6685.

[7] Crichton, W. A.; Bernal, F. L. M.; Guignard, J.; Hanfland, M.; Margadonna, S. Observation of the Sb_2S_3-Type Post-Post-$GdFeO_3$-Perovskite: A Model Structure for High Density ABX_3 and A_2X_3 Phases. arXiv:1410.2783.

[8] Efthimiopoulos, I.; Kemichick, J.; Zhou, X.; Khare, S. V.; Ikuta, D.; Wang, Y. High-Pressure Studies of Bi_2S_3. *J. Phys. Chem. A* **2014**, *118*, 1713−1720.

[9] Sorb, Y. A.; Rajaji, V.; Malavi, P.S.; Subbarao, U.; Hadappa, P.; Karmakar, S.; Peter, S.C.; Narayana,C. Pressure Induced Electronic Topological Transition in Sb_2S_3. *J. Phys.: Condens. Matter* **2016**, *28*, 015602.

[10] Efthimiopoulos, I.; Zhang, J.M.; Kucway, M.; Park, C. Y.; Ewing, R.C.; Wang, Y. Sb_2Se_3 Under Pressure. *Sci. Rep.* **2013**, *3*, 2665-2672.

[11] Lundegaard, L. F.; Miletich, R.; Balic-Zunic, T.; Makovicky, E. Equation of State and Crystal Structure of Sb_2S_3 Between 0 and 10 GPa. *Phys. Chem. Minerals* **2003**, *30*, 463-468.

[12] Lundegaard, L. F.; Makovicky, E.; Boffa-Ballaran, T.; Balic-Zunic, T. Crystal Structure and Cation Lone Electron Pair Activity of Bi_2S_3 Between 0 and 10 GPa. *Phys. Chem. Minerals* **2005**, *32*, 578-584.

[13] Fauth, F.; Peral, I.; Popescu, C.; Knapp, M. The New Material Science Powder Diffraction Beamline at ALBA Synchroton. *Powder Diffr.* **2013**, *28*, S360-S370.

[14] Hammersley, A. P.; Svensson, S. O.; Hanfland, M.; Fitch, A. N.; Häusermann, D. Two-Dimensional Detector Software: From Real Detector to Idealized Image or Two-Theta Scan. *High Pressure Res.* **1996**, *14,* 235−248.

[15] Kraus, W.; Nolze, G. POWDER CELL - A Program for the Representation and Manipulation of Crystal Structures and Calculation of the Resulting X-Ray Powder Patterns. *J. Appl. Crystallogr.* **1996**, *29*, 301−303.

[16] Larson, A. C.; von Dreele, R. B. General Structure Analysis System (GSAS). *LANL Report* **2004**, 86−748.

[17] Toby, B. H. EXPGUI, A Graphical User Interface for GSAS. *J. Appl. Crystallogr.* **2001**, *34*, 210−213.

[18] Mao, H. K.; Xu, J.; Bell, P. M. Calibration of the Ruby Pressure Gauge to 800 kbar Under Quasi-Hydrostatic Conditions. *J. Geophys. Res.* **1986**, *91*, 4673−4676.

[19] Hohenberg, P.; Kohn, W. Inhomogeneous Electron Gas. *Phys. Rev.* **1964**, *136,* B864-B871.

[20] Kresse, G.; Furthmüller. Efficiency of Ab-Initio Total Energy Calculations for Metals and Semiconductors Using a Plane-Wave Basis Set. *Comput. Mater. Sci.* **1996**, *6*, 15-50.

[21] Perdew, J. P.; Ruzsinszky, A.; Csonka, G. I.; Vydrow, O. A.; Suseria, G. E.; Constantin, L. A.; Zhou, X.; Burke, K. Restoring the Density-Gradient Expansion for Exchange in Solids and Surfaces. *Phys. Rev. Lett.* **2008**, *100*, 136406.

[22] Mattsson, A. E.; Armiento, R.; Paier, R. J.; Kresse, G.; Wills, J. M.; Mattsson, T. R. The AM05 Density Functional Applied to Solids. *J. Chem. Phys.* **2008**, *128*, 084714.

[23] Parlinski, K.; Li, Z. Q.; Kawazoe, Y. First-Principles Determination of the Soft Mode in Cubic ZrO_2. *Phys. Rev. Lett.* **1997**, *78*, 4063−4066.

[24] Kyono, A.; Hayakawa, A.; Horiki, M. Selenium Substitution Effect on Crystal Structure of Stibnite (Sb_2S_3). *Phys. Chem. Minerals* **2015**, *42*, 475-490.

[25] Koc, H.; Mamedov, A. M.; Deligoz, E.; Ozisik, H. First Principles Prediction of the Elastic, Electronic, and Optical Properties of Sb_2S_3 and Sb_2Se_3 Compounds. *Solid State Sci.* **2012**, *14*, 1211-1220.

[26] Sereni, P.; Musso, M.; Knoll, P.; Blaha, P.; Schwarz, K. H.; Schmidt, G. Polarization-Dependent Raman Characterization of Stibnite (Sb_2S_3). AIP Conf. Proc. **2010**, *1267*, 1131-1132.

[27] Kharbish, S.; Libowitzky, E.; Beran, A. Raman Spectra of Isolated and Interconnected Pyramidal XS_3 Groups (X = Sb,Bi) in Stibnite, Bismuthinite, Kermesite, Stephanite and Bournonite. *Eur. J. Mineral.* **2009**, *21*, 325-333.

[28] Fan, D. W.; Xu, J. G; Liu, J; Li, Y. C.; Xie, H. S. Thermal Equation of State of Natural Stibnite up to 25.7 GPa and 533 K. *High Temp. High Press.* **2014**, *43*, 351-359.

[29] Zahedi, E.; Xiao, B. DFT Study of Structural, Elastic Properties and Thermodynamic Parameters of Bi_2S_3 Under Hydrostatic Pressures. *Comp. Mat. Sci.* **2015**, *101*, 301-312.

[30] Koc, H.; Ozisik, H.; Deligoz, E.; Mamedov, A. M.; Ozbay, E. Mechanical, Electronic, and Optical Properties of Bi_2S_3 and Bi_2Se_3 Compounds: First Principle Investigations. *J. Mol. Model.* **2014**, *20*, 2180.

[31] Angel, R. J. High-Temperature and High-Pressure Crystal Chemistry. *Book Series: Reviews in Mineralogy & Geochemistry*, **2000**, *41*, 35-60.

[32] Lifshitz, I.M. Anomalies of Electron Characteristics of a Metal in the High Pressure R egion. *Sov. Phys. JETP* **1960**, *11*, 1130-1135.

[33] Blanter, Ya.M.; Kaganov, M.I.; V.S.; Pantsulaya, A.V.; Varlamov, A.A. The Theory of Electronic Topological Transitions. *Phys. Rep.* **1994**, *245*, 159-257.

[34] Varlamov, A.A.; Egorov, V.S.; Pantsulaya, A.V. Kinetic Properties of Metals near Electronic Topological Transitions (21/2-order Transitions). *Adv. Phys.* **1989**, *38*, 469-564.

[35] Manjón, F. J.; Vilaplana, R.; Gomis, O.; Pérez-González, E.; Santamaría-Pérez, D.; Marín-Borrás, V.; Segura, A.; González, J.; Rodríguez-Hernández, P.; Muñoz, A.; et al. High-Pressure Studies of Topological Insulators Bi_2Se_3,Bi_2Te_3, and Sb_2Te_3. *Phys. Status Solidi B* **2013**, *250*, 669-676.

[36] Zhao, K.; Wang, Y.; Sui, Y.; Xin, C.; Wang, X.; Wang, Y.; Liu, Z.; Li, B. First Principles Study of Isostructural Phase Transition in Sb_2Te_3 Under High Pressure. *Phys. Status Solidi RRL* **2015**, *9*, 379-383.

[37] Kikegawa, T.; Iwasaki, H. An X-ray Diffraction Study of Lattice Compression and Phase Transition of Crystalline Phosphorus. *Acta Crystallog. Sect. B* **1983**, 39, 158-164.

[38] Xiang Z.J.; Ye, G.J.; Shang, C.; Wang, N.Z.; Yang, K.S.; Liu, D. Y.; Meng, F.B.; Luo, X.G.; Zou, L.J.; Sun, Z.; et al. Pressure-Induced Electronic Transition in Black Phosphorus. *Phys. Rev. Lett.* **2015**, *115*, 186403.

[39] Pereira, A. L. J.; Sans, J. A.; Vilaplana, R.; Gomis, O.; Manjón, F. J.; Rodríguez-Hernández, P.; Muñoz, A.; Popescu, C.; Beltrán, A. Isostructural Second-Order Phase Transition of β-Bi_2O_3 at High Pressures: An Experimental and Theoretical Study. *J. Phys. Chem. C* **2014**, *118*, 23189-23201.

[40] Vilaplana, R.; Gomis, O.; Manjón, F. J.; Segura, A.; Pérez-González, E.; Rodríguez-Hernández, P.; Muñoz, A.; González, J.; Marín-Borrás, V.; Muñoz-Sanjosé, V.; et al. High-Pressure Vibrational and Optical Study of Bi_2Te_3. *Phys. Rev. B* **2011**, *84*, 104112 (13).

[41] Gomis, O.; Vilaplana, R.; Manjón, F. J.; Rodríguez-Hernández, P.; Pérez-González, E.; Muñoz, A.; Kucek, V.; Drasar, C. Lattice Dynamics of Sb_2Te_3 at High Pressures. *Phys. Rev. B* **2011**, *84*, 174305.

[42] Vilaplana, R.; Santamaría-Pérez, D.; Gomis, O.; Manjón, F. J.; González, J.; Segura, A.; Muñoz, A.; Rodríguez-Hernández, P.; Pérez-González, E.; Marín-Borrás, V.; et al. Structural and Vibrational Study of Bi_2Se_3 Under High Pressure. *Phys. Rev. B* **2011**, *84*, 184110.

[43] Pereira, A. L. J.; Gracia, L.; Santamaría-Pérez, D.; Vilaplana, R.; Manjón, F. J.; Errandonea, D.; Nalin, M.; Beltrán A. Structural and Vibrational Study of Cubic Sb_2O_3 Under High Pressure. *Phys. Rev. B* **2012**, *85*, 174108.

[44] Niilisk, A. I.; Kirs, Y. Y. Influence of a High Hydrostatic Pressure on Photoelectric Properties of Sb_2S_3 and Sb_2Se_3 Single Crystals. *Sov. Phys. Semic.* **1969**, *3*, 11-15.

Table 1. Experimental (exp.) and theoretical (the.) values of atomic parameters of Sb_2S_3 at room pressure. Experimental and theoretical lattice parameters at room conditions are: experiment: a= 11.3049(9), b= 3.8351(3) Å, c= 11.2264(10) Å, theory: $a = 11.2746$ Å, $b = 3.8306$ Å and $c = 10.8941$ Å.

Atom	x	y	z
Sb(1)	0.0294(3) (exp.)	0.25 (exp.)	0.6703(4) (exp.)
	0.1258 (the.)	0.25 (the.)	0.5576 (the.)
Sb(2)	0.3498(3) (exp.)	0.25 (exp.)	0.4633(4) (exp.)
	0.2898 (the.)	0.25 (the.)	0.3083 (the.)
S(1)	0.0514(12) (exp.)	0.25 (exp.)	0.1405(14) (exp.)
	0.0483 (the.)	0.25 (the.)	0.1271 (the.)
S(2)	0.3722(12) (exp.)	0.25 (exp.)	0.0607(12) (exp.)
	0.4761 (the.)	0.25 (the.)	0.1742 (the.)
S(3)	0.2152(12) (exp.)	0.25 (exp.)	0.8039(15) (exp.)
	0.1534 (the.)	0.25 (the.)	0.9679 (the.)

Table 2. Theoretical (the.) and experimental (exp.) Raman mode frequencies and their pressure coefficients in Sb_2S_3 as fitted with equation $\omega(P) = \omega_0 + \alpha P + \beta P^2$. The superscripts indicate different $(B_{1g} + B_{3g})$ and $(B_{2g} + A_g)$ vibrational pairs.

Mode number	Symmetry	ω_0 (the.) (cm^{-1})	α (the.) (cm^{-1}/GPa)	β (the.) (cm^{-1}/GPa^2)	ω_0 (exp.) (cm^{-1})	α (exp.) (cm^{-1}/GPa)	β (exp.) (cm^{-1}/GPa^2)
1	B_{1g}^{1}	43.8	1.72	-0.050			
2	B_{2g}^{1}	44.9	2.10	-0.070	37.5	1.92	-0.020
3	B_{3g}^{1}	46.4	1.84	-0.030			
4	A_{g}^{1}	52.2	1.59	-0.050	51.9	1.42	-0.030
5	B_{1g}^{2}	65.7	2.15	-0.040	60.3	2.60	-0.090
6	B_{3g}^{2}	65.8	2.30	-0.070			
7	A_{g}^{2}	74.7	0.60	-0.070	72.2	1.86	-0.130
8	B_{2g}^{2}	92.9*	6.42*	-			
9	A_{g}^{3}	100	-0.46	0.010	102	-0.005	+0.001
10	B_{2g}^{3}	112*	1.25*	-			
11	B_{2g}^{4}	122*	2.97*	-			
12	A_{g}^{4}	128	4.00	-0.120	129**	3.17	-0.050
13	B_{2g}^{5}	159	9.42	-0.300			
14	A_{g}^{5}	159	7.56	-0.200	158	7.02	-0.150
15	B_{1g}^{3}	182	2.67	-0.002	186**	3.38	-0.050
16	A_{g}^{6}	190	4.94	-0.110	194	3.67	-0.009
17	B_{3g}^{3}	191*	4.10*	-			
18	B_{2g}^{6}	193	5.97	-0.090			
19	B_{3g}^{4}	197*	1.75*	-			
20	B_{1g}^{4}	203	2.45	-0.060			
21	B_{1g}^{5}	225	3.39	-0.060	239	3.49	-0.100
22	B_{3g}^{5}	227	3.46	-0.080			
23	A_{g}^{7}	250*	1.11*	-			
24	B_{2g}^{7}	251	1.61	-0.030			
25	A_{g}^{8}	261*	-0.87*	-			
26	B_{2g}^{8}	278*	-1.06*	0.300	275**	-0.60	-
27	A_{g}^{9}	280	-2.32	0.500	282*	-1.61	0.200
28	B_{2g}^{10}	291*	-2.28*	0.120	299**	-0.17	-
29	A_{g}^{10}	293*	-2.02*	0.400			
30	B_{2g}^{9}	294	1.31	0.080	312	1.90	-0.020

*Values obtained from a fit of low pressure data; **Values extrapolated to zero pressure from a fit of high pressure data.

Table 3. Theoretical (the.) and experimental (exp) values of the room pressure values, the bulk modulus and its pressure derivative of different structural parameters in Sb_2S_3.

	Zero-pressure value	B_0	B_0'
V (the.)	470.4	32.2 GPa	6.2
V (exp.)	486(1) Å^3	37.6(2) GPa	3.8(7)
a (exp.)	11.306(5) Å	21(2) GPa	5.0(7)
b (exp.)	3.835(5) Å	87(2) GPa	4(2)
c (exp.)	11.225(5) Å	35(2) GPa	2.9(5)

Table 4. Experimental axial compresibilities (in units of 10^{-3} GPa^{-1}) of Sb_2S_3, Sb_2Se_3, and Bi_2S_3.

	Sb_2Se_3 [a]	Sb_2S_3 [b]	Bi_2S_3 [c]
χ_a	13.6	15.9(2)	18.7
χ_b	5.0	3.8(1)	4.1
χ_c	9.3	9.5(1)	9.5

[a] Ref. [10], [b] This work, [c] Ref. [12]

Figure captions

Fig. 1. Crystalline structure of orthorhombic (*Pnma*) Sb_2S_3 at ambient pressure (a), at 6.3 GPa (b) and 21.2 GPa (c). The size of the unit cells has been normalized for comparison purposes. Only bonds with lengths below 2.9 Å are shown, which helps us to illustrate the presence of SbS_3 and SbS_5 units at 0 GPa. At pressures above 6 GPa, the former become SbS_6 polyhedra due to the overall reduction of bond lengths. At higher pressures (> 20 GPa), SbS_7 polyhedra are formed at both Sb positions.

Fig. 2. (a) Room-temperature angle-dispersive powder XRD of Sb_2S_3 (empty circles), Rietveld refinement (black solid line), theoretical Bragg reflections (vertical ticks) and residuals from the refinement (red solid line). (b) Raman spectra collected at ambient pressure with theoretical Raman modes (bottom red vertical marks).

Fig. 3. (a) Room-temperature angle-dispersive powder XRD of Sb_2S_3 at selected pressures. Strong signal from Cu shows up in the top pattern, acquired at 10.8 GPa. (b) Rietveld plot corresponding to a XRD pattern measured at 2.9 GPa.

Fig. 4. Experimental (solid dots) and theoretical (solid line) unit-cell volume as a function of pressure for Sb_2S_3. The dashed line shows the result of a fit to the experimental data using the third-order Birch-Murnaghan equation-of-state. The star symbol corresponds to the experimental volume at ambient pressure. Error bars from experimental data are smaller than or equal to the width of the plotted symbols.

Fig. 5. (a) Experimental (solid dots) and theoretical (lines) lattice parameter values as a function of pressure for Sb_2S_3. (b) Experimental (solid dots) and theoretical (solid lines) lattice parameter ratios vs pressure for Sb_2S_3. Star symbols correspond to the experimental data at ambient pressure. Error bars from experimental data are smaller than or equal to the width of the plotted symbols.

Fig. 6. Sketch of the layer structure in Sb_2S_3 and the polyhedral units at ambient pressure. Shortest, medium, and large bond distances inside a layer are represented as solid, long dashed, and short dashed lines, respectively. (a) Experimental (symbols) and theoretical (lines) pressure dependence of the Sb(1) and Sb(2) atomic coordinates in Sb_2S_3. (b) Theoretical pressure dependence of the Sb(1)-S bond lengths. (c) Idem for Sb(2)-S bond lengths. The top left panel shows a sketch of the different Sb-S bonds (<3.1 Å) in Sb_2S_3.

Fig. 7. Room-temperature Raman spectra of Sb_2S_3 at selected pressures.

Fig. 8. Experimental (symbols) and theoretical (lines) pressure dependence of the Raman-mode frequencies of Sb_2S_3. Different colors represent Raman-active modes of different symmetries.

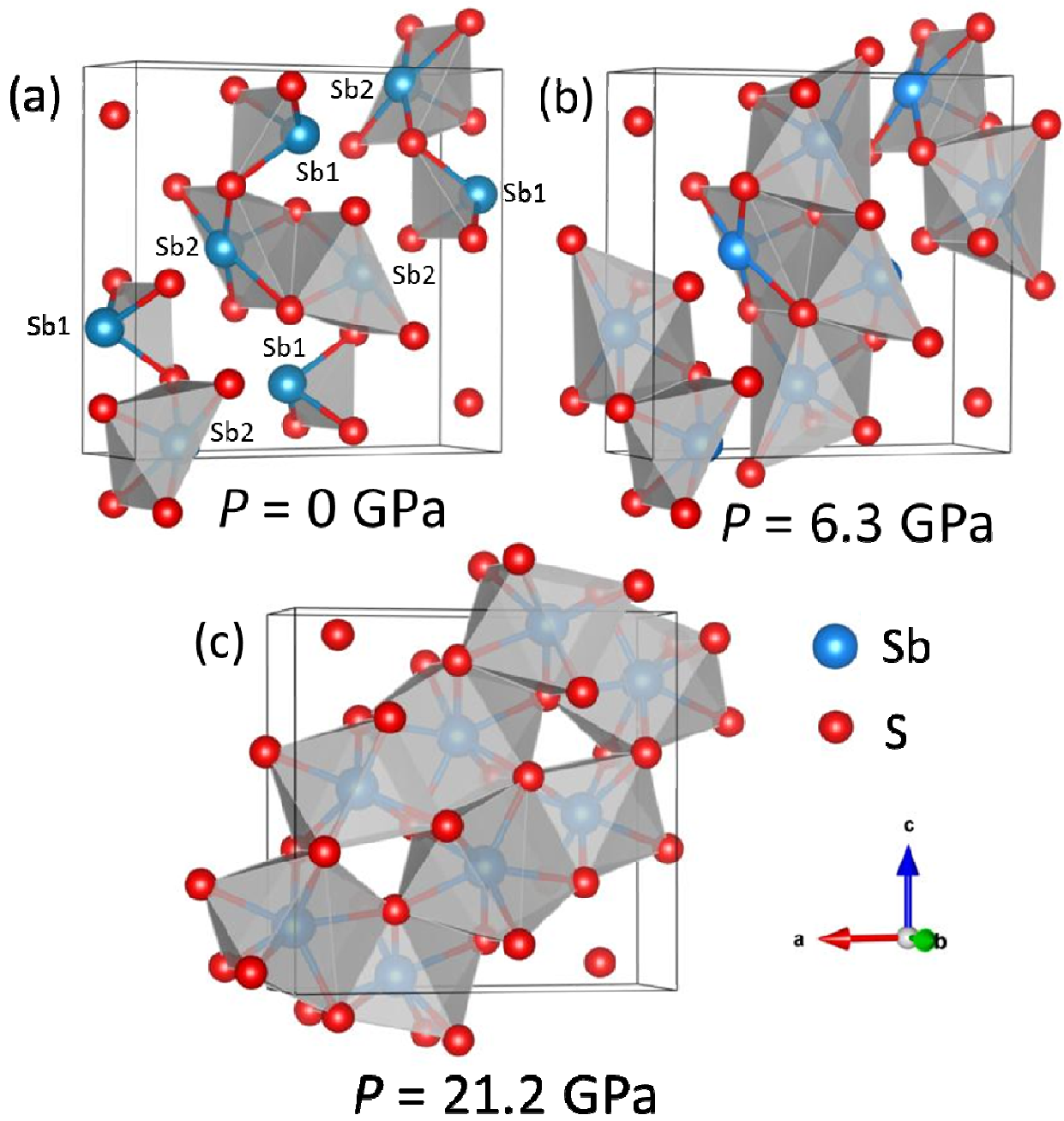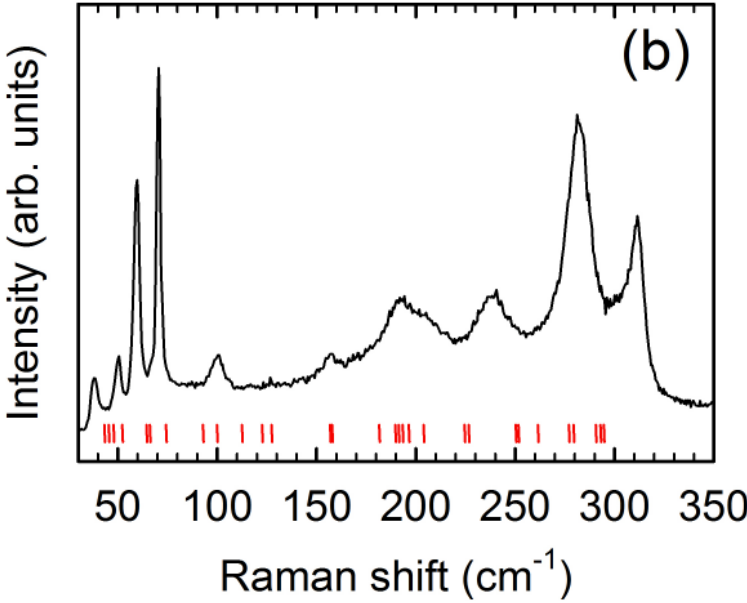**Fig. 9.** Calculated band structure of Sb_2S_3 at 0, 1.0, 3.9 and 6.3 GPa.
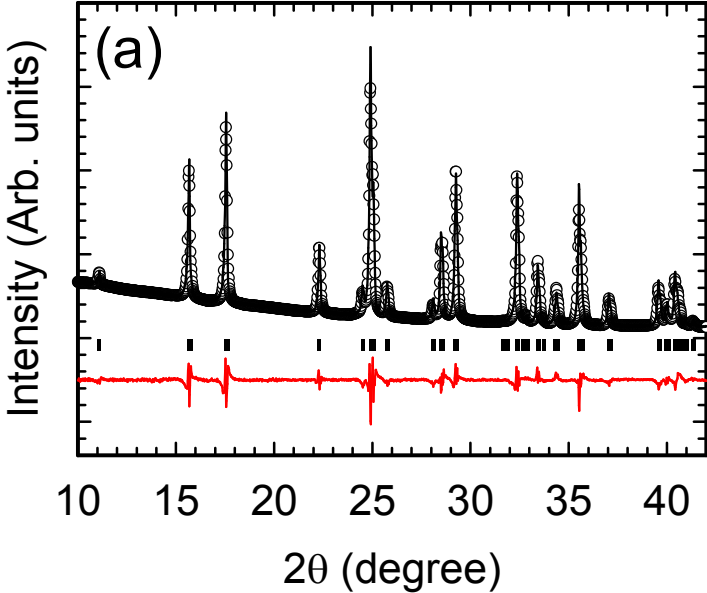
Fig.1

(a) $P = 0$ GPa
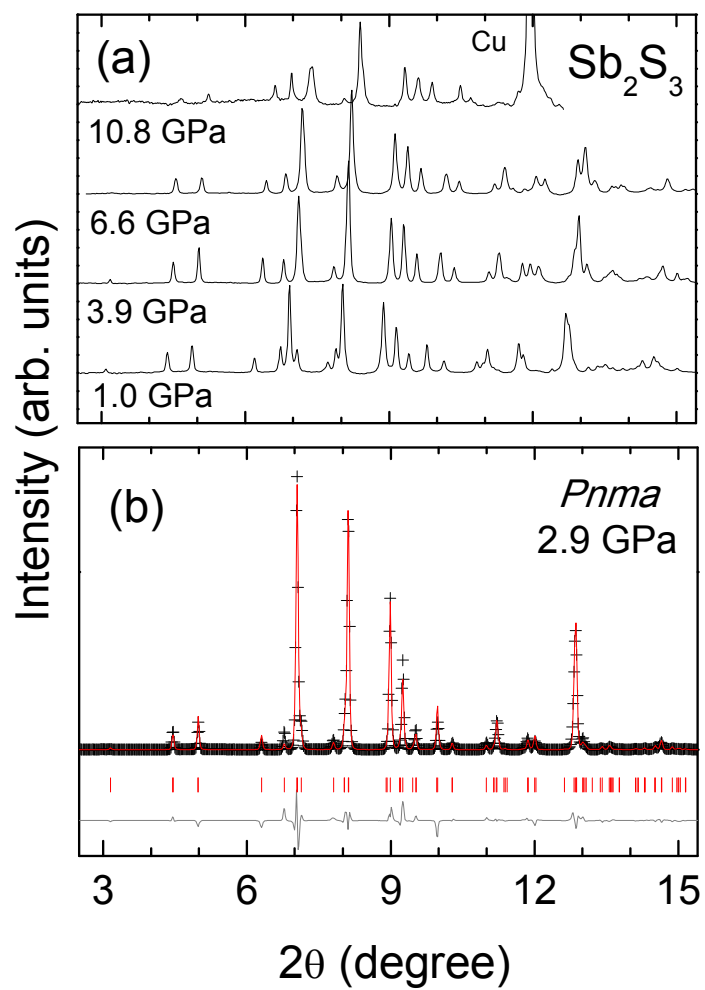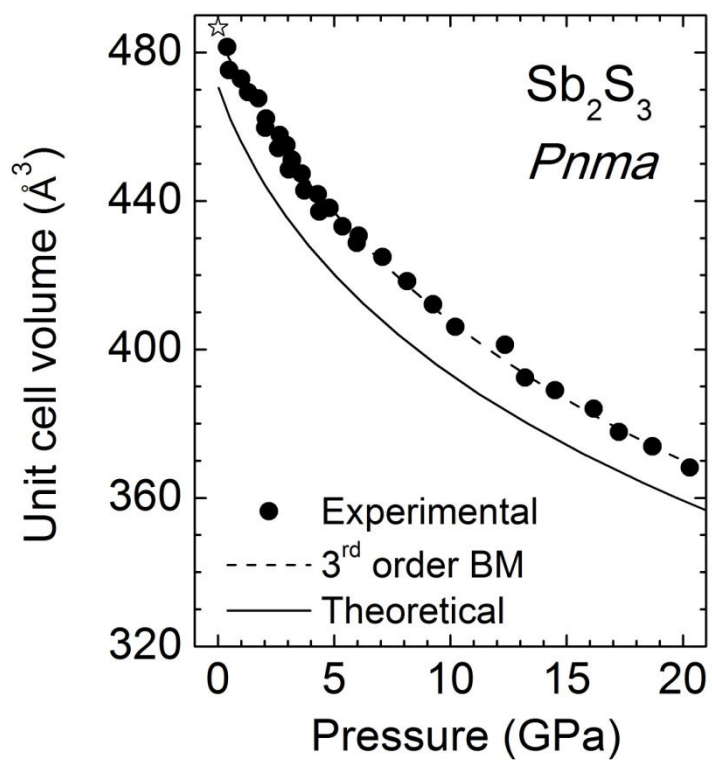
(b) $P = 6.3$ GPa

(c) $P = 21.2$ GPa

Sb

S

Fig. 2

Fig. 3

Fig. 4

Fig. 5

Fig. 6

Sb$_2$S$_3$ (Pnma)

Fig. 7

P (GPa)

1.8

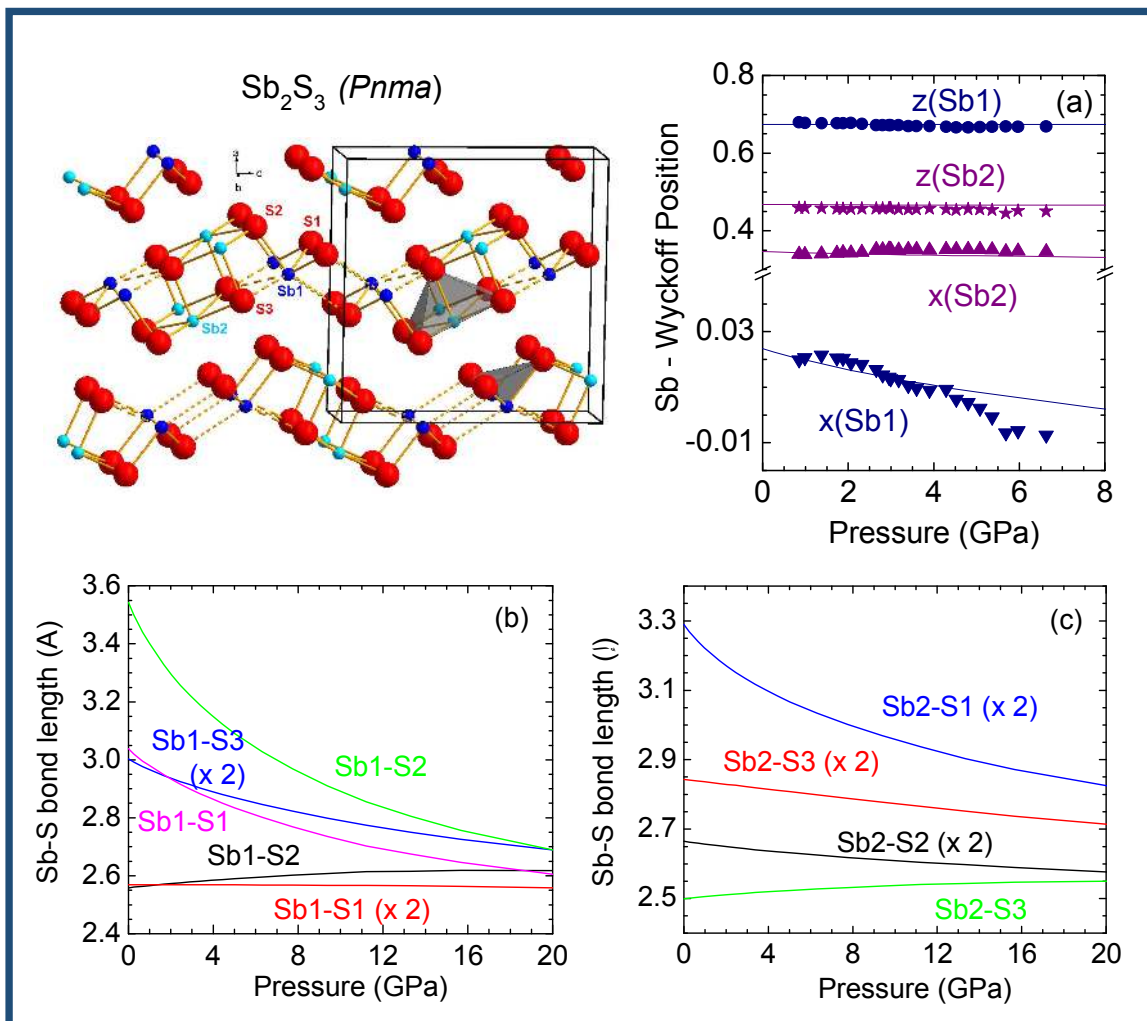4.3

6.4

8.6

10.7

14.7

19.9

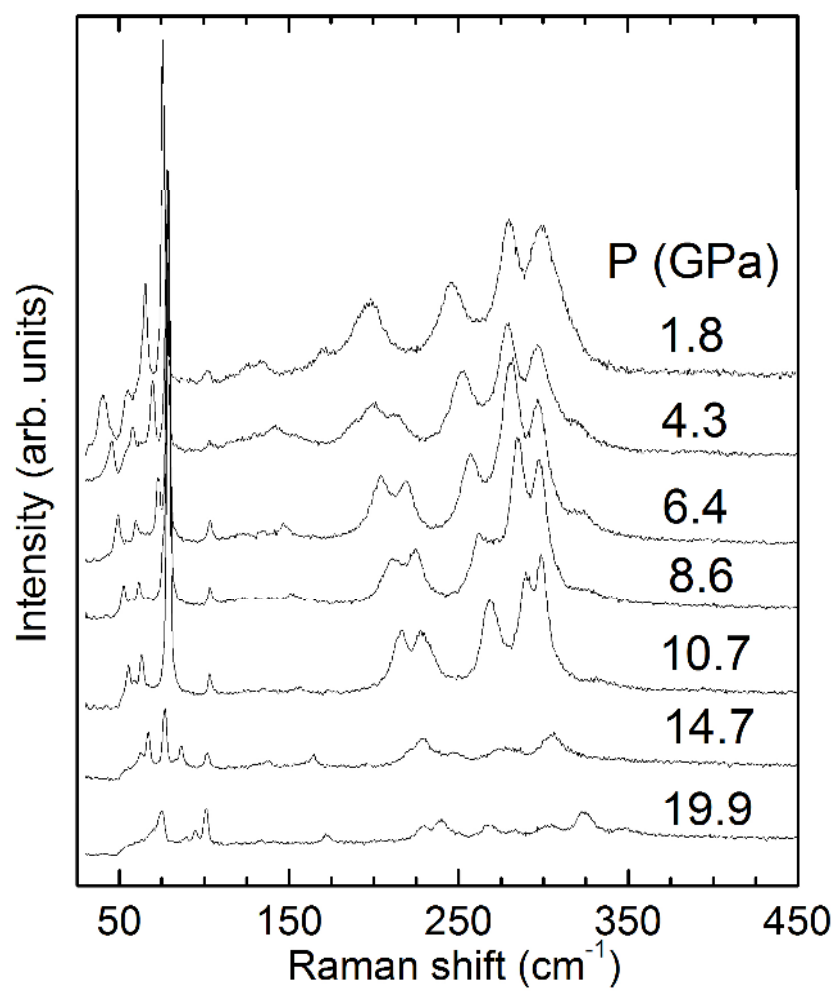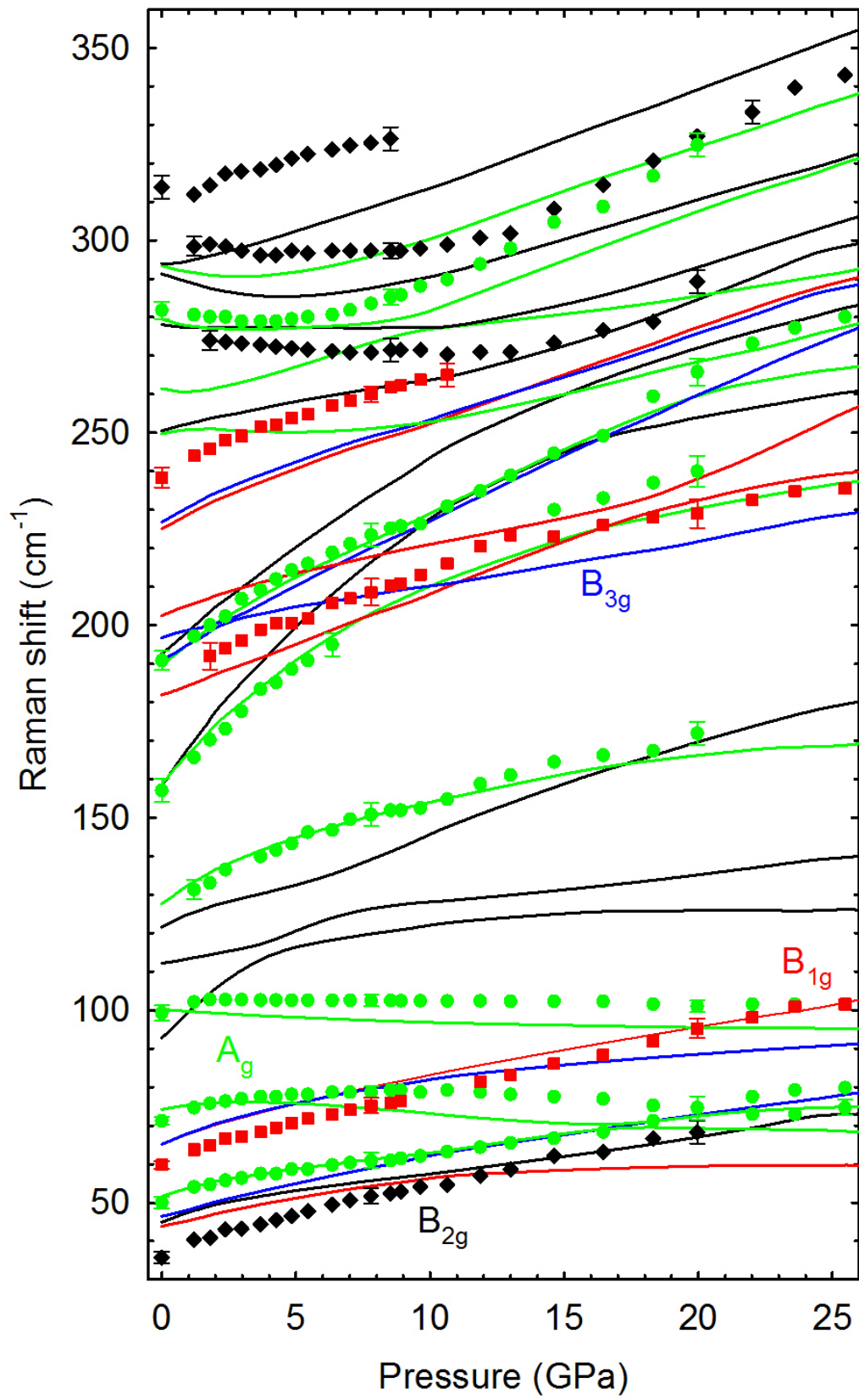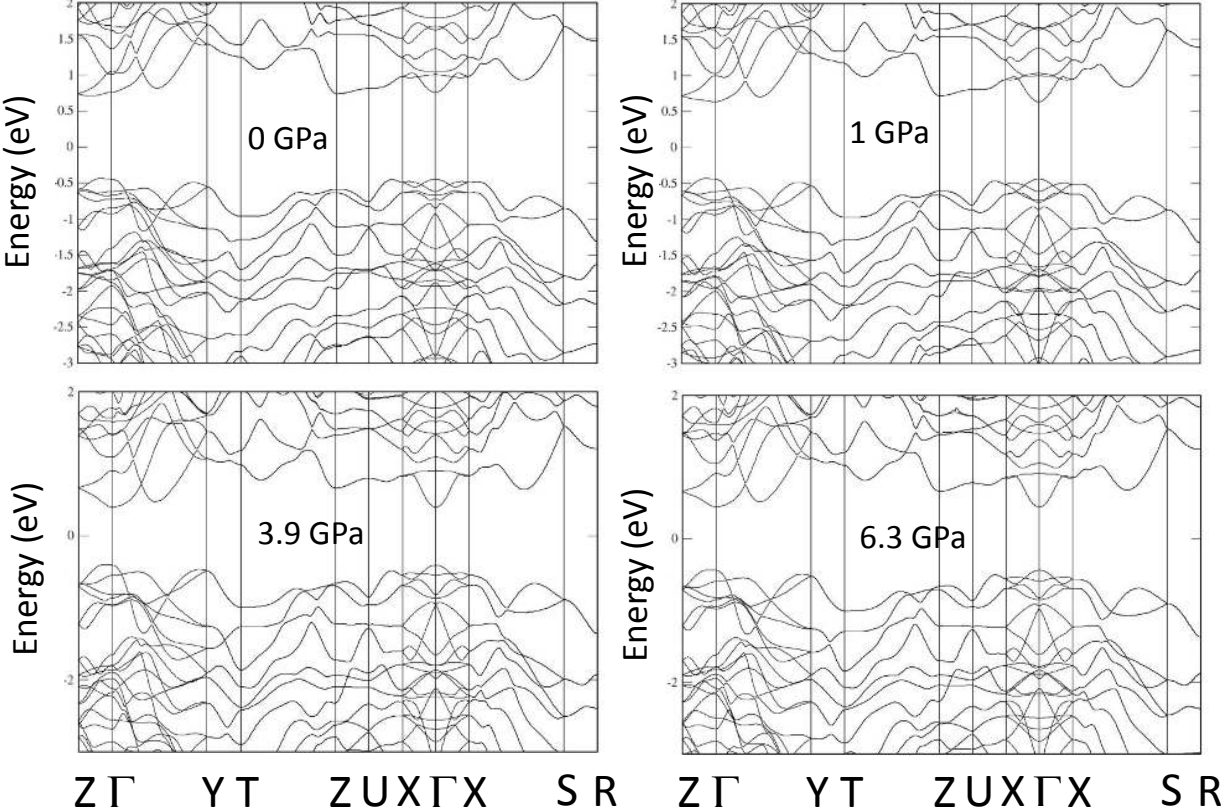Intensity (arb. units)

Raman shift (cm^{-1})
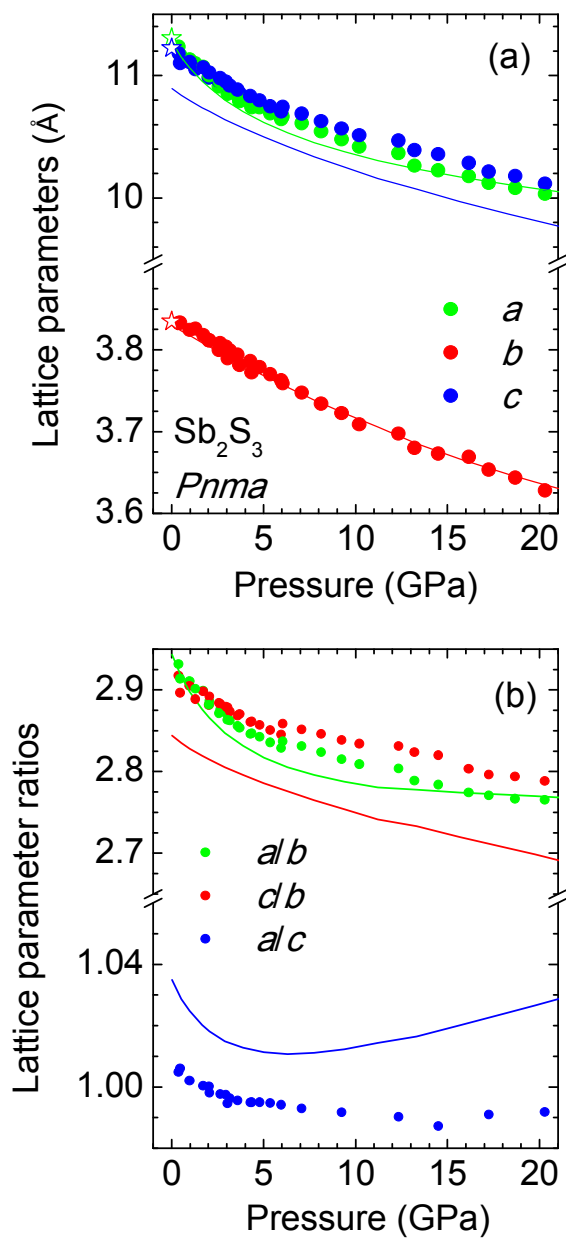
Fig. 8

Fig. 9

Structural, Vibrational, and Electronic Study of Sb₂S₃ at High Pressure

J. Ibáñez,[†] J.A. Sans,[‡] C. Popescu,[§] J. López-Vidrier,[†] J.J. Elvira-Betanzos,[†] V.P. Cuenca-Gotor,[‡] O.Gomis,[°] F.J. Manjón,[*,‡] P. Rodríguez-Hernández,[∥] and A. Muñoz[∥]

[†] Institute of Earth Sciences Jaume Almera, CSIC, 08028 Barcelona, Spain

[‡] Instituto de Diseño para la Fabricación y Producción Automatizada, MALTA Consolider Team, Universitat Politècnica de València, 46022 València, Spain,

[§] ALBA-CELLS, 08290 Cerdanyola del Vallès, Barcelona, Spain

[°] Centro de Tecnologías Físicas: Acústica, Materiales y Astrofísica, MALTA Consolider Team, Universitat Politècnica de València, València, Spain

[∥] Departamento de Física, Instituto de Materiales y Nanotecnología, MALTA Consolider Team, Universidad de La Laguna, 38207 San Cristobal de la Laguna, Tenerife, Spain

Corresponding Author

*E-mail: fjmanjon@fis.upv.es. Telephone: (+34) 963877000 ext (75287).

Supporting Information

S.1. Vibrational properties of Sb₂S₃

In order to understand the lattice dynamics of Sb_2S_3 it is important to remind that the structure of Sb_2S_3 is composed of linked SbS_3E and SbS_5E units, here E refers to the lone electron pair of Sb atoms, since the vibrational modes of chalcogenide compounds have been usually interpreted in a simplified manner in terms of molecular-like units. Within this context, the optical phonons of Sb_2S_3 have been partially interpreted in the past as coming solely from SbS_3 units (without any mention to SbS_5 units) [1,2]. The undistorted SbS_3 units, which have an ideal trigonal pyramidal (C_{3v}) symmetry, give rise to four normal modes of vibration: symmetric stretching $\nu_1(A_1)$, anti-symmetric stretching $\nu_3(E)$, symmetric bending $\nu_2(A_1)$, and anti-symmetric bending $\nu_4(E)$. Koudelka *et al.* estimated the frequencies of SbS_3 units from those measured in $SbCl_3$ molecules and found them to be close to 112, 138, 269, and 302 cm^{-1} [1]. Following similar arguments, the undistorted SbS_5 units, which have an ideal tetragonal pyramidal (C_{4v}) symmetry, give rise to nine normal modes of vibration: axial stretching $\nu_1(A_1)$, antisymmetric in-plane stretching $\nu_4(B_1)$, antisymmetric in-plane stretching+bending

$\nu_7(E)$, symmetric in-plane stretching $\nu_2(A_1)$, antisymmetric in-plane bending $\nu_8(E)$, symmetric in-plane bending $\nu_3(A_1)$, anti-symmetric out-of-plane bending $\nu_5(B_1)$, anti-symmetric in-plane bending $\nu_6(B_2)$ and symmetric in-plane bending $\nu_9(E)$. Stretching modes in distorted tetragonal pyramidal SbS_5 units (similar to those of stibnite) can be observed for instance in $MnSb_2S_4$, with frequency values around 283 and 300 cm^{-1} **[3]**. Despite pure vibrations of SbS_3 units should display considerable higher frequencies (340-380 cm^{-1}) than those observed in $Sb(SR)_3$ molecules **[4,5]**, the vibrational frequencies of $MnSb_2S_4$ have been previously interpreted as due to SbS_3 units instead of distorted SbS_5 units. These arguments suggest that stretching frequencies around 300 cm^{-1} in undistorted SbS_5 units and above 340 cm^{-1} in undistorted SbS_3 units would be expected, which are consistent with the shorter average Sb-S bond distances in SbS_3 units as compared to the SbS_5 units.

To finish this section and just to give an insight of the complex lattice dynamics of Sb_2S_3, we can mention that both SbS_3 and SbS_5 units are linked in stibnite so they have smaller symmetry than in the ideal configuration. This decrease in symmetry leads to splitting of the doubly degenerated E modes of the isolated units. Furthermore, normal vibrations corresponding to SbS_3 and SbS_5 units get mixed in Sb_2S_3, which makes difficult the assignment of the Raman modes. In particular, the link of SbS_3 units with neighboring SbS_3 and SbS_5 units makes impossible the observation of pure symmetric and anti-symmetric stretching modes of SbS_3 units in Sb_2S_3. According to our calculations, the optical mode with the lowest frequency is a silent mode of A_u symmetry with theoretical frequency near 25 cm^{-1} at room pressure. This mode corresponds to the typical shear mode between alternate layers of layered materials. On the contrary, the two highest optical modes are infrared-active modes of B_{1u} and B_{3u} symmetry corresponding to the mixture of a partial symmetric stretching $\nu_1(A_1)$ of SbS_3 units and axial stretching $\nu_1(A_1)$ of SbS_5 units. In fact, the highest Raman active modes are two pairs of $(A_g + B_{2g})$ modes, which correspond to partial anti-symmetric ν_3 stretching of SbS_3 units and ν_8 stretching of SbS_5 units together with partial ν_2 bending of SbS_3 units and ν_1 stretching of SbS_5 units, respectively. This mixture of stretching or stretching and bending modes of SbS_3 and SbS_5 units allows us to explain why the maximum frequency of Raman-active modes in Sb_2S_3 is slightly above 300 cm^{-1} and well below 340 cm^{-1}.

S.2. Calculated lattice parameters and atomic coordinates of Bi_2S_3 and Sb_2Se_3.

Table S1. Experimental (exp.) and theoretical (the.) values of atomic positions of Bi_2S_3 at room pressure. Experimental and theoretical lattice parameters are: experiment: a= 11.269(2), b= 3.9717(3) Å, c= 11.129(2) Å (from **Ref. 6**), theory: $a = 11.40958$ Å, $b = 3.9680$ Å and $c = 11.0068$ Å.

Atom	x	y	z
Bi(1)	0.0164(2) (exp.)	0.25 (exp.)	0.6745(2) (exp.)
	0.0149 (the.)	0.25 (the.)	0.6750 (the.)
Bi(2)	0.3406(3) (exp.)	0.25 (exp.)	0.4661(2) (exp.)
	0.3608 (the.)	0.25 (the.)	0.4638 (the.)
S(1)	0.0494(16) (exp.)	0.25 (exp.)	0.1311(11) (exp.)
	0.0476 (the.)	0.25 (the.)	0.1294 (the.)
S(2)	0.3773(17) (exp.)	0.25 (exp.)	0.0604(12) (exp.)
	0.3768 (the.)	0.25 (the.)	0.0554 (the.)
S(3)	0.2165(16) (exp.)	0.25 (exp.)	0.8069(12) (exp.)
	0.2142 (the.)	0.25 (the.)	0.8080 (the.)

Table S2. Experimental (exp.) and theoretical (the.) values of atomic positions of Sb_2Se_3 at room pressure. Experimental and theoretical lattice parameters are: experiment: a= 11.80, b= 3.97 Å and c= 11.65 Å (from **Ref. 7**), theory: $a = 11.7968$ Å, $b = 3.9818$ Å and $c = 11.2831$ Å.

Atom	x	y	z
Sb(1)	0.4971(1) (exp.)	0.25 (exp.)	0.8228(3) (exp.)
	0.5226 (the.)	0.25 (the.)	0.8290 (the.)
Sb(2)	0.3432(1) (exp.)	0.25 (exp.)	0.4559(2) (exp.)
	0.3499 (the.)	0.25 (the.)	0.4624 (the.)
Se(1)	0.7162(2) (exp.)	0.25 (exp.)	0.7105(3) (exp.)
	0.7149 (the.)	0.25 (the.)	0.6966 (the.)
Se(2)	0.5597(3) (exp.)	0.25 (exp.)	0.3673(2) (exp.)
	0.5536 (the.)	0.25 (the.)	0.3667 (the.)
Se(3)	0.3675(2) (exp.)	0.25 (exp.)	0.0629(3) (exp.)
	0.3706 (the.)	0.25 (the.)	0.0521 (the.)

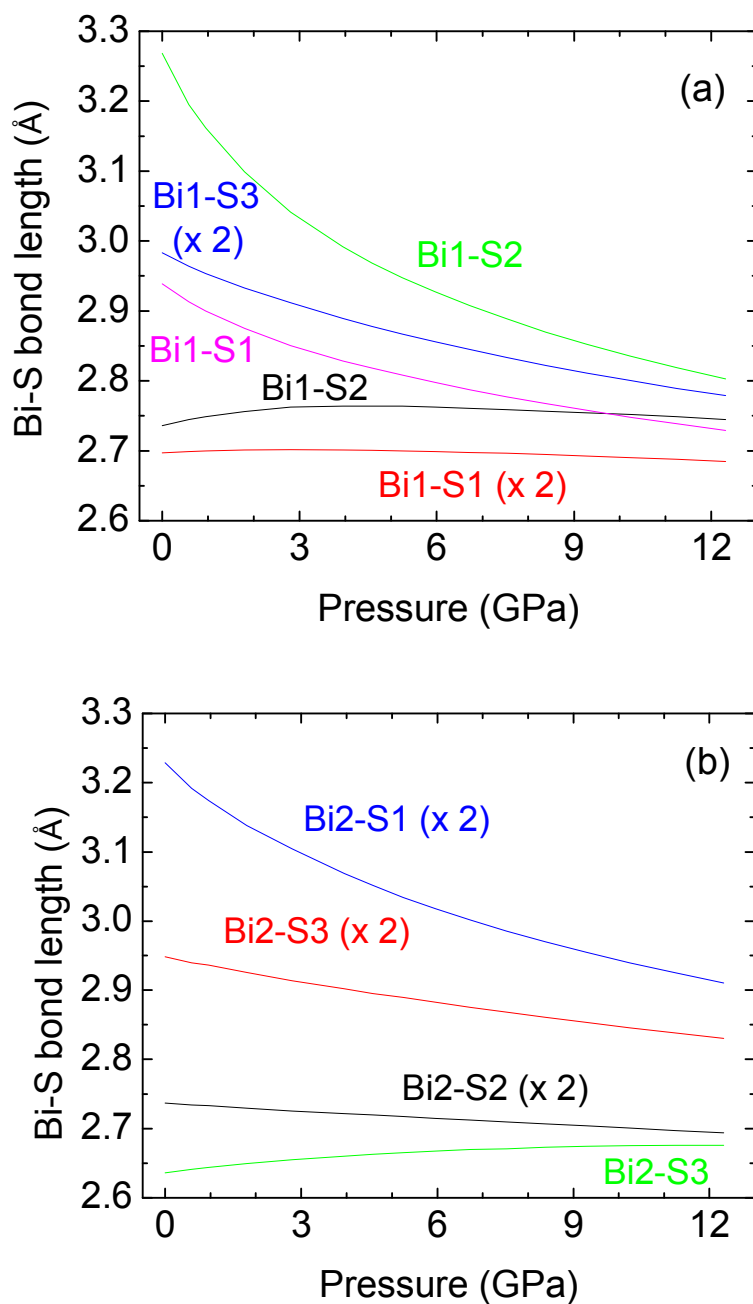**S.3. Pressure dependence of bond-lengths in Bi$_2$S$_3$ and Sb$_2$Se$_3$.**

Fig. S1 (a) Theoretical pressure dependence of the Bi(1)-S bond lengths in Bi$_2$S$_3$. (b) Idem for the Bi(2)-S bond lengths.
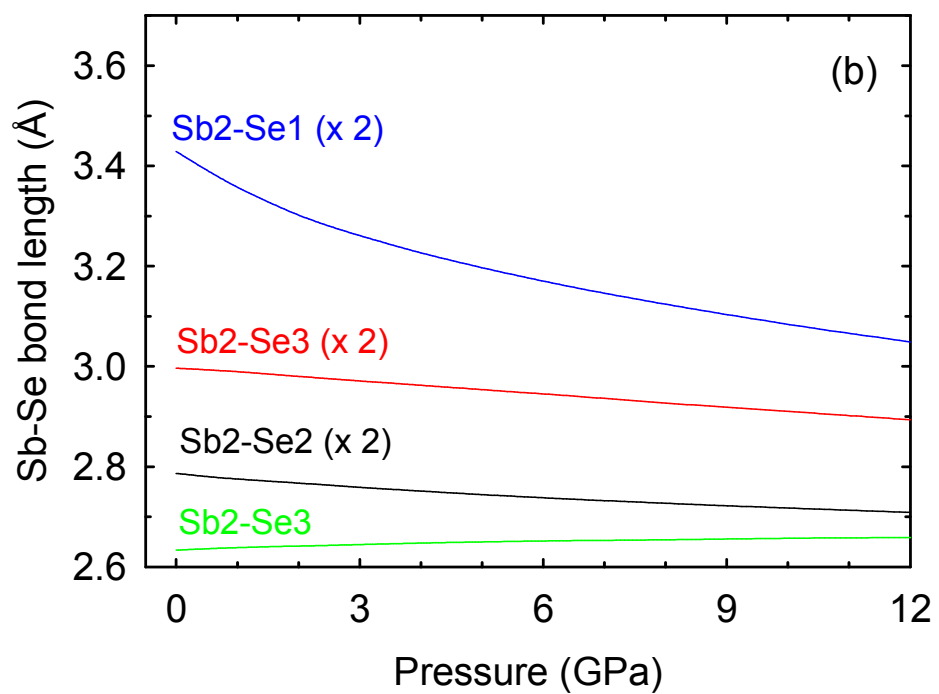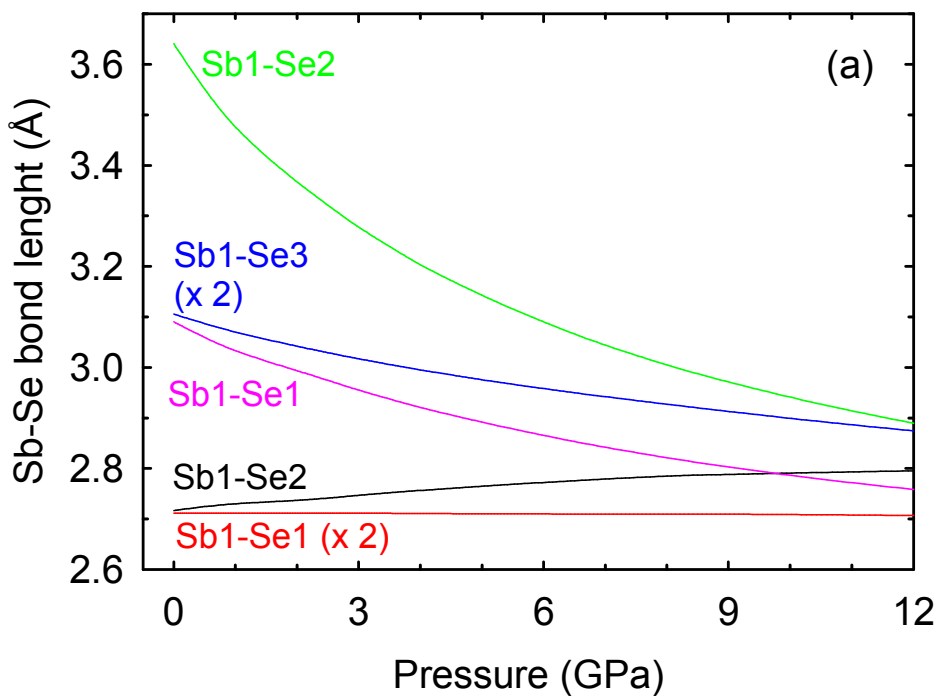
Fig. S2 (a) Theoretical pressure dependence of the Sb(1)-Se bond lengths in Sb₂Se₃. (b) Idem for the Sb(2)-Se bond lengths.

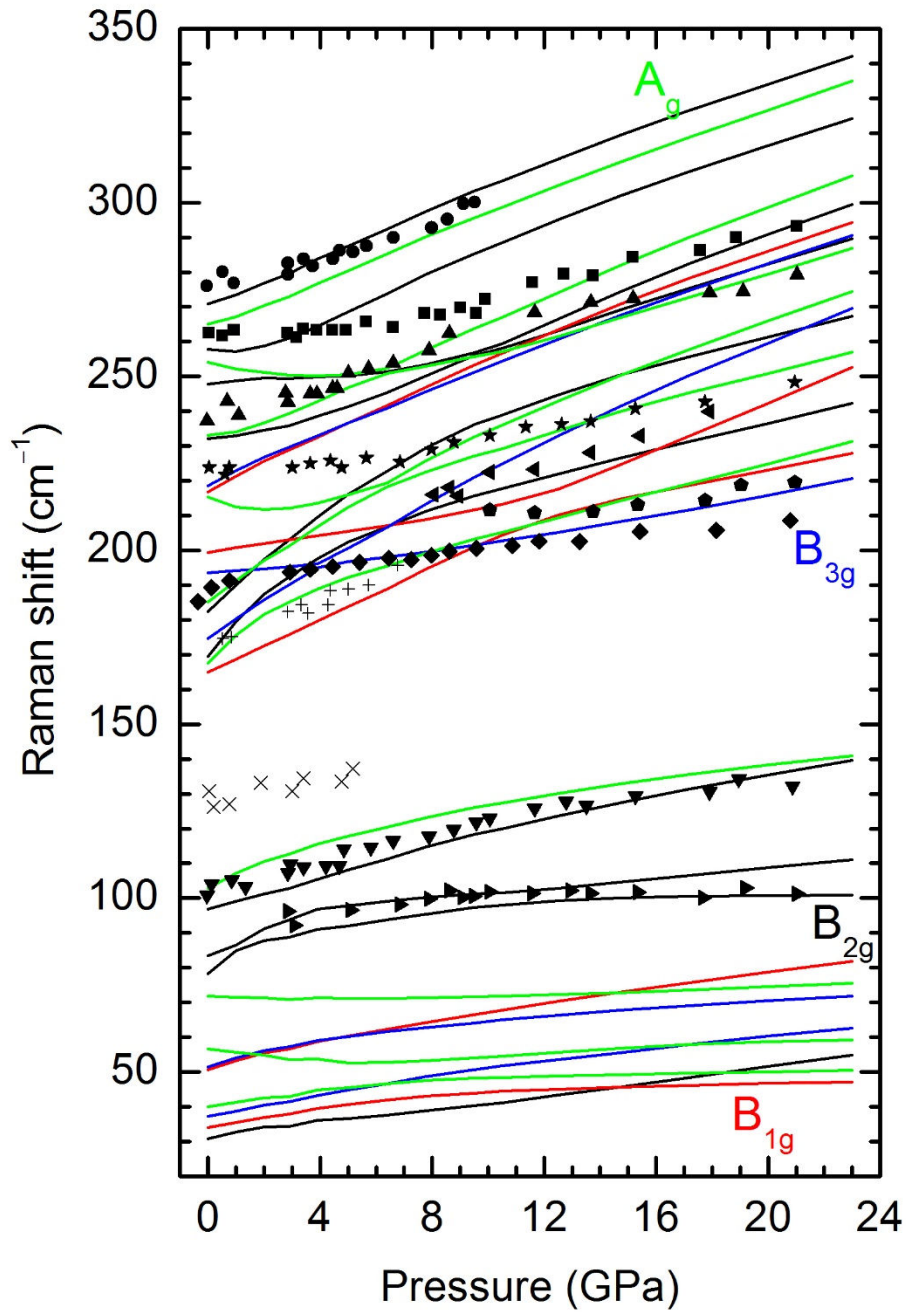### S.4. Pressure dependence of Raman-active modes in Bi₂S₃ and Sb₂Se₃.

Fig. S3 Experimental (symbols) and theoretical (lines) pressure dependence of the Raman-mode frequencies of Bi₂S₃. Different colors represent Raman-active modes of different symmetries.
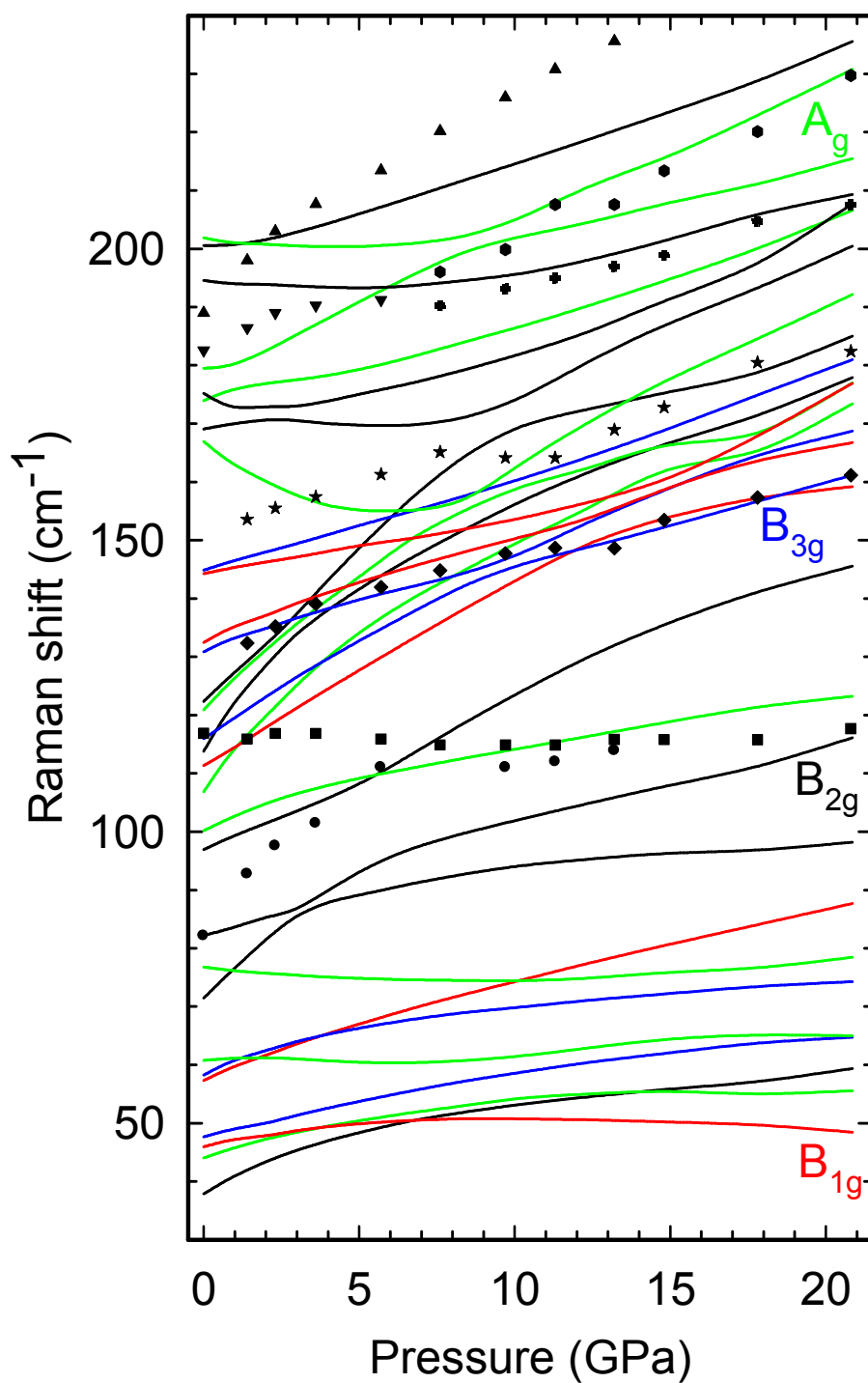
Fig. S4 Experimental (symbols) and theoretical (lines) pressure dependence of the Raman-mode frequencies of Sb_2Se_3. Different colors represent Raman-active modes of different symmetries.

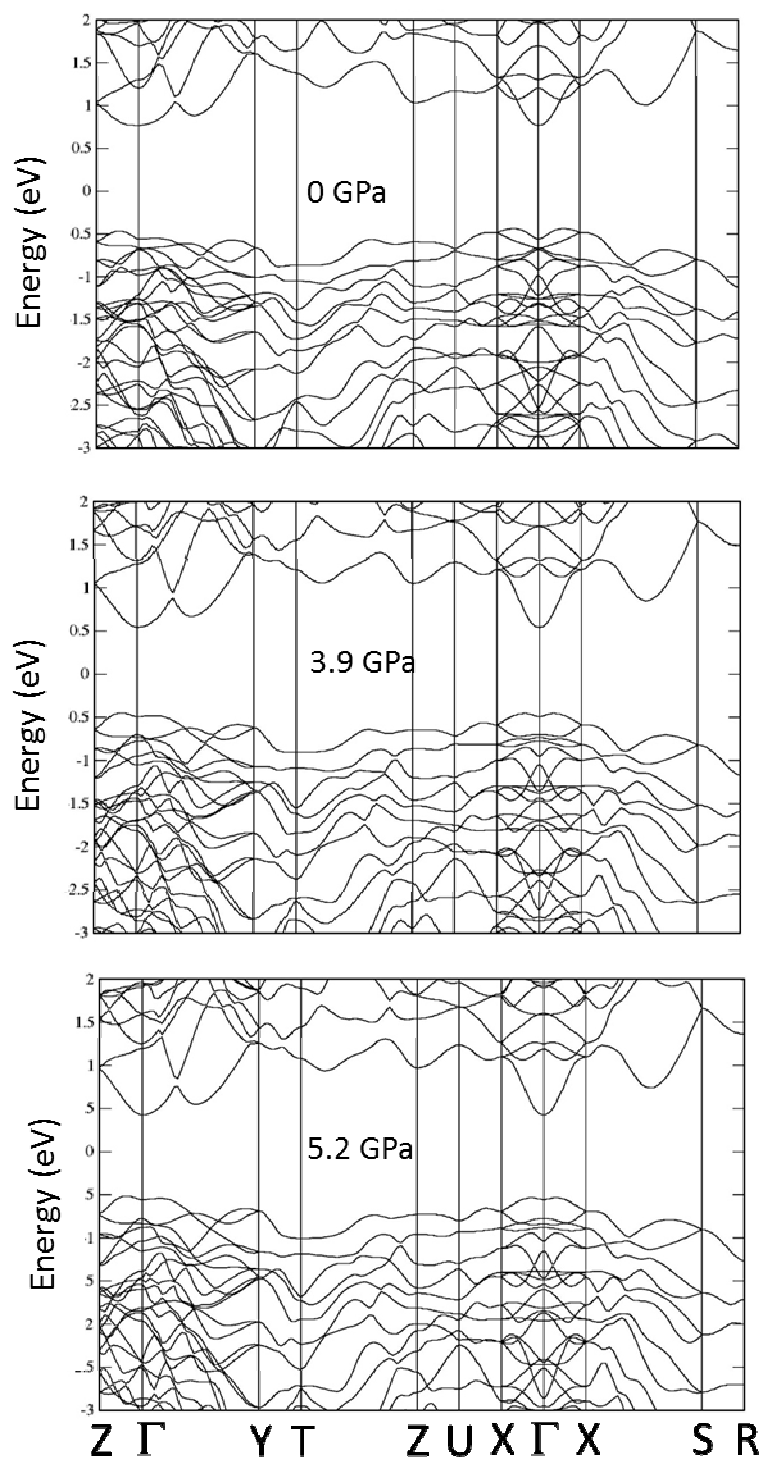**S.5. Pressure dependence of electronic band structure in Bi₂S₃ and Sb₂Se₃.**

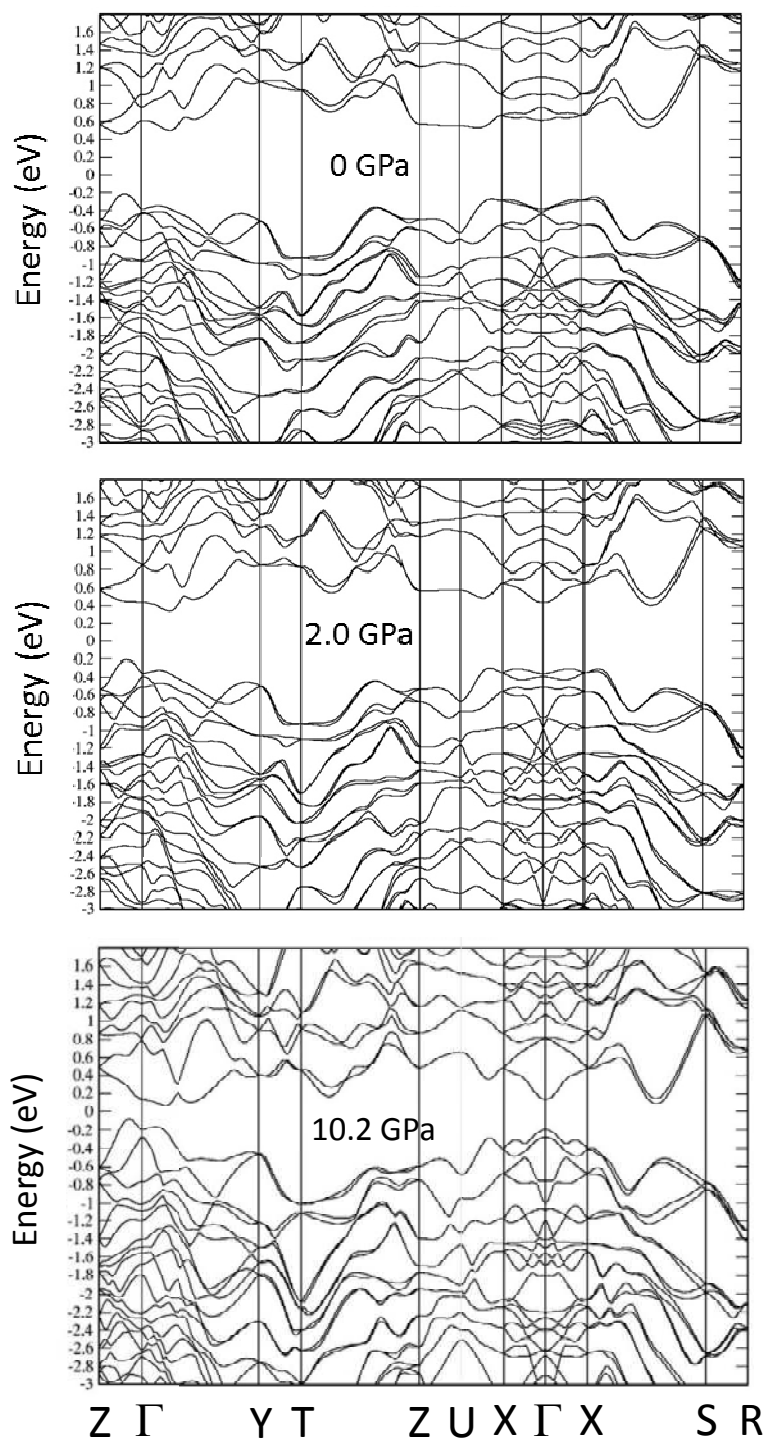**Fig. S5** Calculated electronic band structure of Bi₂S₃ at 0, 3.9 and 5.2 GPa.

Fig. S6 Calculated electronic band structure of Sb$_2$Se$_3$ at 0, 2.0, and 10.2 GPa.

Bibliography

[1] Koudelka, L.; Horak, J.; Pisarcik, M. Raman Spectra of the $(GeS_2)_{1-x}(Sb_2S_3)_x$ System. *Chem. Zvesti* **1981**, *35*, 327-332.

[2] Kharbish, S.; Libowitzky, E.; Beran, A. Raman Spectra of Isolated and Interconnected Pyramidal XS_3 Groups (X = Sb,Bi) in Stibnite, Bismuthinite, Kermesite, Stephanite and Bournonite. *Eur. J. Mineral.* **2009**, *21*, 325-333.

[3] Pfizner A.; Kurowski, D. A New Modification of $MnSb_2S_4$ Crystallizing in the $HgBi_2S_4$ Structure Type. *Z. Kristall.* **2009**, *215*, 373-376.

[4] Pfizner, A. Copper Iodide as Solid Solvent for Thiometalate Ions. *Chem. Eur. J.* **1997**, *3*, 2032-2038.

[5] Weidlein, J.; Müller, U.; Dehnicke, K.; Schwingungsfrequenzen I. Thieme, Stuttgart, **1981,** p. 155.

[6] Lundegaard, L. F.; Makovicky, E.; Boffa-Ballaran, T.; Balic-Zunic, T. Crystal Structure and Cation Lone Electron Pair Activity of Bi_2S_3 between 0 and 10 GPa. *Phys. Chem. Minerals* **2005**, *32*, 578-584.

[7] Efthimiopoulos, I.; Zhang, J.M.; Kucway, M.; Park, C. Y.; Ewing, R.C.; Wang, Y. Sb_2Se_3 Under Pressure. *Sci. Rep.* **2013**, *3*, 2665-2672.